



**HAL**  
open science

## The thermal properties of hydrothermally altered andesites from La Soufrière de Guadeloupe (Eastern Caribbean)

Michael J Heap, David E Jessop, Fabian B Wadsworth, Marina Rosas-Carbajal, Jean-Christophe Komorowski, H Albert Gilg, Nadège Aron, Margaux Buscetti, Laura Gential, Margaux Goupil, et al.

### ► To cite this version:

Michael J Heap, David E Jessop, Fabian B Wadsworth, Marina Rosas-Carbajal, Jean-Christophe Komorowski, et al.. The thermal properties of hydrothermally altered andesites from La Soufrière de Guadeloupe (Eastern Caribbean). *Journal of Volcanology and Geothermal Research*, 2022, 421, 10.1016/j.jvolgeores.2021.107444 . hal-03480233

**HAL Id: hal-03480233**

**<https://uca.hal.science/hal-03480233>**

Submitted on 4 Feb 2022

**HAL** is a multi-disciplinary open access archive for the deposit and dissemination of scientific research documents, whether they are published or not. The documents may come from teaching and research institutions in France or abroad, or from public or private research centers.

L'archive ouverte pluridisciplinaire **HAL**, est destinée au dépôt et à la diffusion de documents scientifiques de niveau recherche, publiés ou non, émanant des établissements d'enseignement et de recherche français ou étrangers, des laboratoires publics ou privés.

1 The thermal properties of hydrothermally altered andesites from La  
2 Soufrière de Guadeloupe (Eastern Caribbean)

3

4 **Michael J. Heap<sup>1,2\*</sup>, David E. Jessop<sup>3,4,5</sup>, Fabian B. Wadsworth<sup>6</sup>, Marina Rosas-Carbajal<sup>3</sup>,**  
5 **Jean-Christophe Komorowski<sup>3</sup>, H. Albert Gilg<sup>7</sup>, Nadège Aron<sup>1</sup>, Margaux Buscetti<sup>1</sup>, Laura**  
6 **Gential<sup>1</sup>, Margaux Goupil<sup>1</sup>, Mathilde Masson<sup>1</sup>, Lucie Hervieu<sup>1</sup>, Alexandra R.L. Kushnir<sup>1</sup>,**  
7 **Patrick Baud<sup>1</sup>, Lucille Carbillet<sup>1</sup>, Amy G. Ryan<sup>8</sup>, and Roberto Moretti<sup>3,4</sup>**

8

9 <sup>1</sup> *Université de Strasbourg, CNRS, Institut Terre et Environnement de Strasbourg, UMR 7063,*  
10 *5 rue Descartes, Strasbourg F-67084, France*

11 <sup>2</sup> *Institut Universitaire de France (IUF), Paris, France*

12 <sup>3</sup> *Université de Paris, Institut de Physique du Globe de Paris, CNRS UMR 7154, F-75005 Paris,*  
13 *France*

14 <sup>4</sup> *Observatoire Volcanologique et Sismologique de Guadeloupe, Institut de Physique du Globe*  
15 *de Paris, F-97113 Gourbeyre, France*

16 <sup>5</sup> *CNRS, IRD, OPGC Laboratoire Magmas et Volcans, Université Clermont Auvergne, F-63000,*  
17 *Clermont-Ferrand, France*

18 <sup>6</sup> *Earth Science, Durham University, Science Labs, Durham, DL1 3LE, United Kingdom*

19 <sup>7</sup> *Engineering Geology, TUM School of Engineering and Design, Technical University of*  
20 *Munich, 80333 Munich, Germany*

21 <sup>8</sup> *Department of Earth and Environmental Sciences, University of Minnesota, MN 55455, USA*

22

23 \*Corresponding author: Michael Heap (heap@unistra.fr)

24

25 **Abstract**

26           The heat flux of an active volcano provides crucial information on volcanic unrest. The  
27 hydrothermal activity often responsible for volcanic unrest can be accompanied by an increase  
28 in the extent and intensity of hydrothermal alteration, which could influence the thermal  
29 properties of the volcanic edifice. Therefore, an understanding of the influence of alteration on  
30 the thermal properties of rocks is required to better interpret volcano heat flux data. We provide  
31 laboratory measurements of thermal conductivity, thermal diffusivity, and specific heat  
32 capacity for variably altered (intermediate to advanced argillic alteration) andesites from La  
33 Soufrière de Guadeloupe (Eastern Caribbean). We complement these data with previously  
34 published data for altered basaltic-andesites from Merapi (Indonesia) and new data for altered  
35 rhyodacites from Chaos Crags (USA). Our data show that thermal conductivity and thermal  
36 diffusivity decrease as a function of increasing porosity, whereas the specific heat capacity does  
37 not change systematically. Thermal conductivity decreases as a function of alteration (the  
38 percentage of secondary minerals) for the rocks from La Soufrière and Merapi (from  $\sim 1.6$  to  
39  $\sim 0.6 \text{ W}\cdot\text{m}^{-1}\cdot\text{K}^{-1}$  as alteration increases from  $\sim 1.5$  to  $>75$  wt.%), but increases for the rocks from  
40 Chaos Crags (from  $\sim 1.1$  to  $\sim 1.5 \text{ W}\cdot\text{m}^{-1}\cdot\text{K}^{-1}$  as alteration increases from  $\sim 6$  to  $\sim 15$  wt.%).  
41 Although the thermal diffusivity of the rocks from Chaos Crags increases from  $\sim 0.65$  to  
42  $\sim 0.75\text{--}0.95 \text{ mm}^2\cdot\text{s}^{-1}$  as alteration increases from  $\sim 6$  to  $\sim 15$  wt.%, the thermal diffusivity of the  
43 rocks from La Soufrière and Merapi does not appear to be greatly influenced by alteration. The  
44 specific heat capacity is not significantly affected by alteration, although there is a slight trend  
45 of increasing specific heat capacity with alteration for the rocks from La Soufrière. We conclude  
46 that the decrease in thermal conductivity as a function of alteration in the rocks from La  
47 Soufrière and Merapi is the result of the low conductivity of the secondary mineral assemblage,  
48 and that a combination of the high thermal conductivity of cristobalite and the reduction in  
49 porosity as a result of the void-filling mineral precipitation can explain the increase in thermal  
50 conductivity in the rocks from Chaos Crags. Calculations show that an increase in alteration of

51 a dome or edifice can result in decreases and increases in heat flow density, depending on the  
52 type of alteration. Therefore, alteration-induced changes in the thermal properties of dome or  
53 edifice rocks should be considered when interpreting volcano heat flux data. We conclude that  
54 it is important not only to monitor the extent and evolution of alteration at active volcanoes, but  
55 also the spatial distribution of alteration type.

56

57 **Keywords:** heat flux; alteration; porosity; thermal conductivity; thermal diffusivity; specific  
58 heat capacity; Merapi; Chaos Crags

59

60 **Highlights:**

- 61 • Hydrothermal alteration changes the thermal properties of volcanic rocks.
- 62 • Alteration can increase or decrease thermal properties, depending on alteration type.
- 63 • Alteration can change the conductive heat flow density at a volcano.
- 64 • Alteration should be considered when interpreting volcano heat flux data.

65

## 66 **1 Introduction**

67 Active volcanoes, and particularly those with very active hydrothermal systems, emit a  
68 prodigious amount of heat (Wright and Flynn, 2004). The heat from magma at depth is  
69 transported to the surface by a combination of mechanisms, including the movement of magma,  
70 the advection (e.g., by convection) of hot fluids, and the conduction of heat through rock.  
71 Because changes in the heat emitted by a volcano can indicate the movement of magma and/or  
72 modifications to the hydrothermal system, monitoring heat flux at active volcanoes provides  
73 crucial information on volcanic activity and unrest (Jessop et al., 2021). Indeed, heat flux has  
74 been measured, or is continuously monitored, at volcanoes worldwide (Dehn et al., 2001;  
75 Wright et al., 2004), including Whakaari (New Zealand; Bloomberg et al., 2014), Vulcano

76 (Italy; Mannini et al., 2019), Campi Flegrei (Italy; Chiodini et al., 2005), Kīlauea (USA; Harris  
77 et al., 2001), Mt Etna (Italy; Harris et al., 1997), Volcán de Colima (Mexico; Stevenson and  
78 Varley, 2008), Lascar (Chile, Wooster and Rothery, 1997), and La Soufrière de Guadeloupe  
79 (Eastern Caribbean; Jessop et al., 2021). The link between the thermal output of a volcano and  
80 volcanic activity was recently emphasised by Girona et al. (2021), who highlighted that large-  
81 scale thermal unrest was a reliable indicator of impending magmatic and phreatic eruptions.

82         The thermal properties of volcanic rocks comprising the edifice or dome, and processes  
83 that increase or decrease these properties, are therefore informative for those charged with  
84 interpreting surficial heat flux data at volcanoes. Furthermore, the thermal properties of  
85 volcanic rocks are also an important input parameter in a wide range of models, such as those  
86 designed to model heat loss from magma chambers, conduits, sills, dykes, lavas, and  
87 ignimbrites (Irvine, 1970; Norton and Knight, 1977; Carrigan, 1984; Bruce and Huppert, 1989;  
88 Carrigan et al., 1992; Fialko and Rubin, 1999; Wooster et al., 1997; Annen et al., 2008; Nabelek  
89 et al., 2012; Heap et al., 2017a; Annen, 2017; Mattsson et al., 2018; Tsang et al., 2019). In  
90 general, for simplicity, the thermal properties of rocks in and around volcanoes are often taken  
91 to be constant, which facilitates calculations of heat flow and how it changes with, for example,  
92 hydrothermal circulation or magma movement. And yet, laboratory data show that thermal  
93 properties are variable with porosity (e.g., Robertson and Peck, 1974) and temperature (e.g.,  
94 Whittington et al., 2009).

95         For the reasons given above, there is a clear outstanding need to better understand the  
96 evolution of thermal properties as other rock characteristics change. This endeavour is well  
97 suited to laboratory investigation in which the thermal properties of volcanic rocks are  
98 constrained (Horai et al., 1970; Fujii and Osako, 1973; Robertson and Peck, 1974; Bagdassarov  
99 and Dingwell, 1994; Whittington et al., 2009; Romine et al., 2012; Mielke et al., 2015, 2016,  
100 2017; Vélez et al., 2018; Heap et al., 2020a; Weydt et al., 2021). For example, the thermal

101 conductivity of variably porous basalt from Hawai'i (USA) was found to decrease from  $\sim 1.7$   
102  $\text{W}\cdot\text{m}^{-1}\cdot\text{K}^{-1}$  at a porosity  $\sim 0.05$  down to  $\sim 0.2 \text{ W}\cdot\text{m}^{-1}\cdot\text{K}^{-1}$  at a porosity of  $\sim 0.85$  (Robertson and  
103 Peck, 1974). The average thermal conductivities of andesite (average porosity of 0.095) and  
104 rhyolite lava (average porosity of 0.275) from the Tauhara geothermal field (New Zealand)  
105 were measured to be 1.32 and 1.11  $\text{W}\cdot\text{m}^{-1}\cdot\text{K}^{-1}$ , respectively (Mielke et al., 2015), and the  
106 thermal conductivities of andesite (porosity of 0.023–0.130), dacite (porosity of 0.108), and  
107 rhyolite (porosity of 0.231) from the Taupō Volcanic Zone (New Zealand) were measured to  
108 be 1.19–1.70, 1.18, and 1.04  $\text{W}\cdot\text{m}^{-1}\cdot\text{K}^{-1}$ , respectively (Mielke et al., 2016). More recently,  
109 Heap et al. (2020a) measured the thermal properties (thermal conductivity, thermal diffusivity,  
110 and specific heat capacity) of variably porous andesites from Mt Ruapehu (New Zealand) and  
111 variably altered basaltic-andesites from Merapi volcano (Indonesia). The thermal conductivity  
112 of low-porosity ( $\sim 0.05$ ) samples from Mt Ruapehu was measured to be between  $\sim 1.4$  and  $\sim 1.6$   
113  $\text{W}\cdot\text{m}^{-1}\cdot\text{K}^{-1}$ , but decreased to  $\sim 0.4 \text{ W}\cdot\text{m}^{-1}\cdot\text{K}^{-1}$  at a porosity of  $\sim 0.6$  (Heap et al., 2020a). These  
114 authors also found that saturation with water increased the bulk specific heat capacity and  
115 thermal conductivity, and decreased the thermal diffusivity, relative to the dry state. Thermal  
116 property measurements on samples from Merapi volcano suggested that hydrothermal  
117 alteration decreases thermal conductivity and thermal diffusivity, and increases specific heat  
118 capacity (Heap et al., 2020a).

119         Despite these laboratory studies, and others, our understanding of the thermal properties  
120 of volcanic rocks stands to benefit from new laboratory data. In particular, little is known about  
121 the influence of hydrothermal alteration on the thermal properties of volcanic rocks. However,  
122 an understanding as to how hydrothermal alteration can influence thermal properties is  
123 important. This is because increasing volcanic unrest resulting in an elevated heat flux, which  
124 is linked to impending magmatic and phreatic eruptions (Girona et al., 2021), is often associated  
125 with a visible increase in alteration (Jessop et al., 2021). Here, we report findings from a

126 laboratory study designed to better understand the influence of hydrothermal alteration on the  
127 thermal properties of volcanic rocks, using La Soufrière de Guadeloupe as a case study volcano.  
128

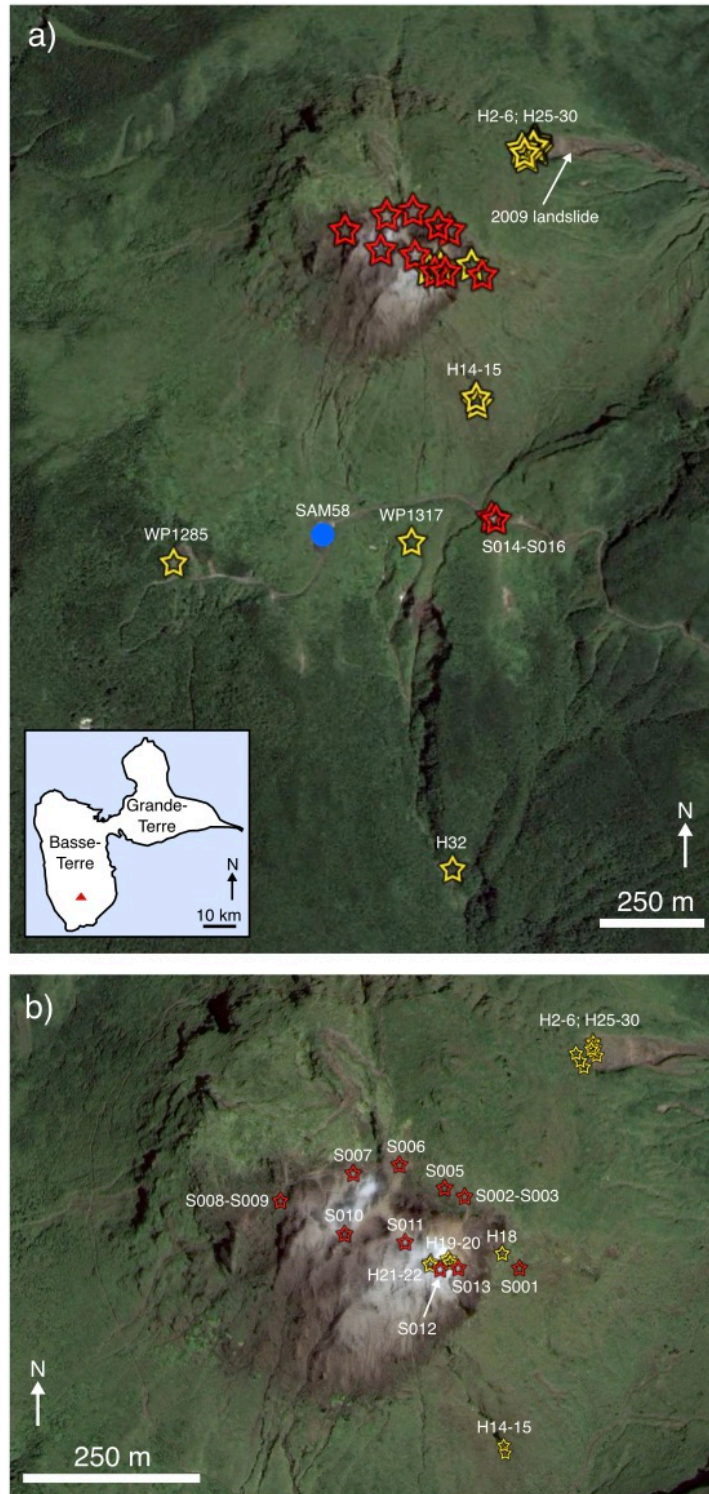
## 129 **2 La Soufrière de Guadeloupe (Eastern Caribbean)**

130       La Soufrière de Guadeloupe (hereafter called La Soufrière) is an active andesitic  
131 stratovolcano located on the island of Guadeloupe in the Eastern Caribbean (Figure 1a). There  
132 have been six non-magmatic phreatic or hydrothermal eruptions at La Soufrière since 1635 CE,  
133 the largest and most-recent eruption of which occurred in 1976–1977 (Komorowski et al.,  
134 2005). The 1976–1977 volcanic crisis resulted in the evacuation of ~70,000 people and severe  
135 socio-economic consequences for the island of Guadeloupe (Feuillard et al., 1983; Hincks et  
136 al., 2014; Komorowski et al., 2005, 2015). Volcanic unrest has been increasing at La Soufrière  
137 since 1992, manifest as (1) the formation of new fumaroles and an expansion of the outgassing  
138 area on top of the lava dome (Brombach et al., 2000; Komorowski et al., 2005; Villemant et al.,  
139 2014; Allard et al., 2014; Moretti et al., 2020), (2) the appearance of high-flow-rate thermal  
140 acid sulfate-chloride springs on the slopes and at the base of the dome (Villemant et al., 2005;  
141 2014), (3) an increase in the heat output from the dome (Gaudin et al., 2013; Jessop et al., 2021),  
142 (4) an increase in seismic activity (hundreds of shallow, low-magnitude earthquakes each  
143 month) and the largest felt volcano-tectonic earthquake since 1976–1977 (Moretti et al., 2020),  
144 and (5) large flank displacements (Moretti et al., 2020; Heap et al., 2021a).

145       Activity within the shallow hydrothermal system, which has been imaged by a variety  
146 of geophysical methods (Nicollin et al., 2006; Brothelande et al., 2014; Bouligand et al., 2016;  
147 Rosas-Carbajal et al., 2016), is considered responsible for much of the recent volcanic unrest  
148 (Moretti et al., 2020; Heap et al., 2021a). Indeed, La Soufrière has a history of unrest associated  
149 with hydrothermal activity. Not only were hydrothermally altered rocks ejected from the vent  
150 during the 1976–1977 crisis (Feuillard et al., 1983), but geological evidence have also suggests

151 that historic partial edifice collapses at La Soufrière were associated with hydrothermal activity,  
152 owing to the abundance of hydrothermally altered materials in debris avalanche deposits  
153 (Boudon et al., 1987; Komorowski et al., 2005; Le Friant et al., 2006; Salaün et al., 2011; Rosas-  
154 Carbajal et al., 2016; Peruzzetto et al., 2019). Because the tropical climate of the island of  
155 Guadeloupe (i.e. high yearly precipitation) contributes to dome washout and the shallow  
156 hydrothermal regime, La Soufrière represents an ideal natural laboratory to study the influence  
157 of hydrothermal alteration on the thermal properties of a nearly fluid-saturated volcanic dome.  
158 Further, and importantly, such data are timely due to the link between magmatic and phreatic  
159 eruptions and the increase in heat output associated with increased hydrothermal activity at the  
160 volcano (Moretti et al., 2020; Jessop et al., 2021; Girona et al., 2021).

161



162

163 **Figure 1.** (a) Map of La Soufrière de Guadeloupe (Eastern Caribbean; taken from Google

164 Earth®) showing the sampling locations for the 19 rock blocks of the main sample suite

165 (yellow stars; the “H” series), the 3 rock blocks and 13 bags of unlithified material from the

166 second field campaign (red stars; the “S” series), and the borehole rock sample (blue circle;

167 SAM58). Inset shows a map of Guadeloupe in which the location of La Soufrière de  
168 Guadeloupe is indicated by a red triangle. (b) Zoom of the dome summit area showing the  
169 sampling sites on the dome (also taken from Google Earth®).

170

### 171 **3 Materials and Methods**

172 Materials (rock blocks and unlithified deposits) were collected over two field campaigns  
173 conducted at La Soufrière in 2019. The main sample suite of 19 rock blocks were collected  
174 during the first field campaign (“H” series), which were supplemented by 3 rock blocks and 13  
175 bags of unlithified material collected during the second campaign (“S” series). The sampling  
176 locations are provided in Figure 1. Our aim was to sample a range of materials from different  
177 locations on the volcano that best represent the observed variability in porosity and  
178 hydrothermal alteration.

179 Of the 19 rock blocks from the main sample suite, the “H” series, nine blocks were taken  
180 from the collapse scar of the 2009 landslide (H2A, H2B, H3, H4A, H5A, H6, H25, H29, and  
181 H30). Five blocks were collected from the dome summit: four blocks were taken from the lava  
182 spines of the 1530 CE dome (two blocks from *Cratère Sud Central*, H19 and H20, and two  
183 blocks from an adjacent site, H21 and H22), and one block was taken from the *Lacroix*  
184 *Supérieure* outgassing fracture (H18). We also collected blocks from the West wall of the fault  
185 *Faille 30 août* (H14 and H15), the collapse scar of the landslide triggered by the 21 November  
186 2004 *Les Saintes* magnitude Mw 6.3 regional earthquake (Feuillet et al., 2011) (WP1285), and  
187 adjacent to the *Galion* waterfall (H32). The final block, a volcanic bomb from the 1976–1977  
188 eruption, was taken from the roof of a small disused thermal bathhouse to the South of the dome  
189 (WP1317).

190 Samples in the “S” series were mostly tephra (millimetric granular matter in an argillic  
191 matrix). Out of the 16 samples collected, only S005, S008, and S016 were rock blocks. S001

192 was taken from just below the summit plateau to the East of the dome. Notably, this location is  
193 upwind of the predominant wind direction and thus the sample was relatively uncontaminated  
194 by fumarolic gases. Samples S002–S006 were taken from within the thermally-active zone  
195 (called “ZFNN” in Jessop et al., 2021), but from locations mostly unaffected by strong  
196 outgassing. S007 was taken directly downwind and from the rim of the *Tarrisan* crater. Samples  
197 S008–S011 were taken from various sites downwind of the main outgassing sites, and samples  
198 S012 and S013 were collected in proximity to the main outgassing vents. Finally, samples  
199 S014–S016 were taken from the base of the volcano, close to a site with low-level, passive  
200 degassing and highly-altered soils due to historical high-activity. An additional rock sample  
201 was taken from a borehole (SAM58) located at the *Savane à Mulets* carpark on the southwest  
202 base of the dome (Figure 1a). This sample was taken from a depth of ~58 m.

203 Multiple cylindrical samples were cored from each of the rock blocks (from the “H” and  
204 “S” series) to a diameter of 20 mm, and then cut and precision-ground to a nominal length of  
205 40 mm. The samples were washed and then dried in a vacuum-oven at 40 °C for at least 48 h.  
206 The connected porosity of each sample was calculated using the bulk sample volume and the  
207 skeletal (solid) sample volume measured by a helium pycnometer. The cylindrical samples  
208 prepared from each block were then grouped into pairs of similar porosity. For most blocks,  
209 three pairs of samples were measured. For certain blocks (H15, H30, SAM58, S005, S008, and  
210 S016), which were smaller, only two pairs of samples were measured.

211 The unlithified materials were first sieved to a grain diameter < 2 mm and then dried in  
212 a vacuum-oven at 40 °C for at least 48 h. The solid density of each unlithified sample was then  
213 measured using the mass and volume, measured by a helium pycnometer, of an aliquot of the  
214 oven-dry powder.

215 The thermal conductivity,  $\lambda$  (in units of  $\text{W}\cdot\text{m}^{-1}\cdot\text{K}^{-1}$ ), and thermal diffusivity,  $D$  (in units  
216 of  $\text{mm}^2\cdot\text{s}^{-1}$ ), were measured using a Hot Disk® TPS 500 Thermal Constants Analyser using the

217 transient plane source method (Gustafsson, 1991; Gustavsson et al., 1994; Harlé et al., 2019;  
218 Heap et al., 2020a). The transient plane source method is a periodic method to measure the  
219 thermal properties of materials (Hofmeister, 2019). The standard uncertainties for thermal  
220 conductivity and thermal diffusivity values using the transient hot-strip method, arising from  
221 contact losses and ballistic radiative transfer gains (Hofmeister, 2019), were determined to be  
222 2.6 and 11%, of the measured values respectively (Hammerschmidt and Sabuga, 2000).

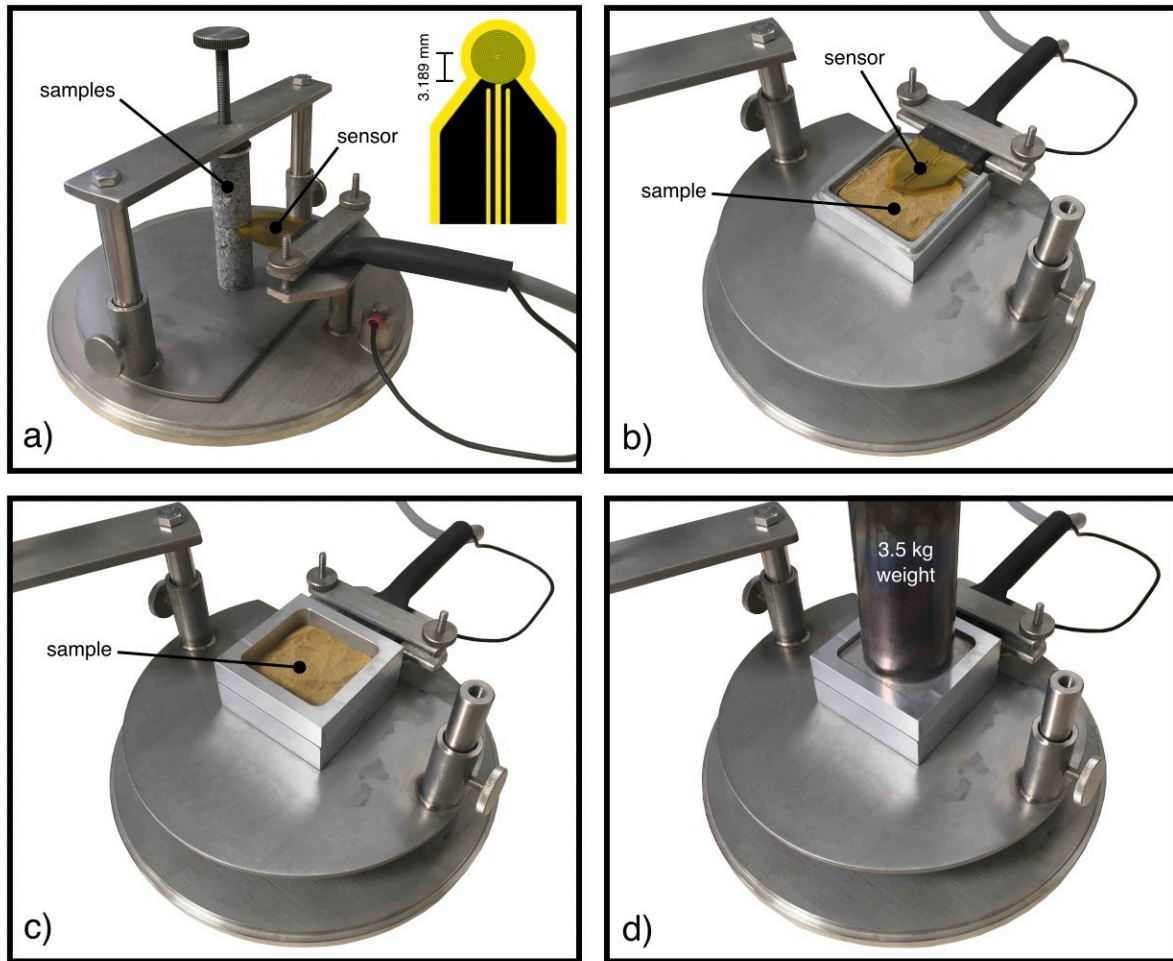
223 Thermal conductivity and thermal diffusivity were measured using a sensor consisting  
224 of two 10  $\mu\text{m}$ -thick nickel foil spirals (radius of 3.189 mm) that are encased and insulated by  
225 30  $\mu\text{m}$ -thick kapton (see inset on Figure 2a). For the rock samples, the sensor was sandwiched  
226 between two cylindrical samples, of similar porosity, cored from the same block (Figure 2a).  
227 The rock samples were held in place using a screw positioned at the top of the sample jig (Figure  
228 2a), which ensured good contact between the sensor and the surface of the samples.

229 The unlithified samples were measured using a sample holder of known volume  
230 supplied by Hot Disk®. Powder was first spooned into the lower part of the sample holder, and  
231 the sensor was placed on top of the powder (Figure 2b). The top part of the sample holder was  
232 then placed on top of the lower part, and more powder was spooned on top of the sensor (Figure  
233 2c). A plate was then placed on top of the sample assembly, and the entire sample assembly  
234 was compacted using a 3.5 kg weight (Figure 2d). The 3.5 kg weight ensured (1) a similar  
235 compaction from sample to sample and (2) a good contact between the powder and the sensor.

236 The temperature adjacent to the sample, measured using a thermocouple, was inputted  
237 into the Thermal Constants Analyser prior to starting each measurement. An electrical current  
238 of known power and duration was passed through the sensor during the measurement, which  
239 also recorded the increase in sample temperature as a function of time. The output power and  
240 duration required for a reliable measurement varied from sample to sample and were found  
241 using trial-and-error. The output power and test duration were typically 100–200 mW and 5–

242 10 s, respectively. Four consecutive measurements were performed on each pair of samples (on  
243 the four different combinations of sample end-faces) and each powder, and we report herein an  
244 average of these four measurements. Each measurement was performed at least five minutes  
245 apart to ensure that the sample had cooled back to the ambient temperature. The sensor  
246 measured the temperature drift of the sample for 40 seconds prior to each measurement to check  
247 whether the sample was in thermal equilibrium. If the sample temperature was not constant  
248 during this 40 second period, the data were not considered and the measurement was repeated.  
249 Following each set of measurements on the powder samples, the mass of the powder was  
250 measured to provide the bulk sample density and, using the solid density of each powder, their  
251 total porosities were calculated. The volumetric heat capacity,  $\rho_b c_p$  (in units of  $\text{J}\cdot\text{m}^{-3}\cdot\text{K}^{-1}$ ),  
252 calculated by the Hot Disk® device, was divided by the independently determined bulk sample  
253 density,  $\rho_b$ , to provide the bulk sample specific heat capacity,  $c_p$  (in units of  $\text{J}\cdot\text{kg}^{-1}\cdot\text{K}^{-1}$ ). All  
254 measurements were conducted in a far-field environment that was at ambient laboratory  
255 temperature and pressure.

256



257

258 **Figure 2.** (a) Photograph of the experimental setup for the rock-rock measurements.

259 Insets show the sensor used, consisting of two 10  $\mu\text{m}$ -thick nickel foil spirals (radius of 3.189

260 mm) that are encased and insulated by 30  $\mu\text{m}$ -thick kapton (used for all measurements). The

261 screw on the top of the setup ensures a good contact between the sensor and the samples.

262 Panels (b), (c), and (d) are photographs that show the procedure for measuring a powder

263 sample. (b) The powder was first spooned into the lower part of the holder, underneath the

264 sensor. (c) The upper part of the holder was placed onto the lower part and powder was

265 spooned over the sensor. (d) The top of the holder (a flat piece) was placed on top of the

266 powder and a 3.5 kg weight was placed on top of the setup to ensure reproducible

267 compaction and a good contact between the sensor and the powder.

268

269 Polished thin sections were prepared from offcuts of the main sample suite (the “H”  
270 series) for microstructural analysis using a Tescan Vega 2 XMU scanning electron microscope  
271 (SEM). The mineral contents of 17 of the 19 blocks from the “H” series, collected during the  
272 first field campaign, were quantified using X-ray powder diffraction (XRPD) in Heap et al.  
273 (2021a). We provide here the mineral contents of the two remaining samples from this sample  
274 suite (samples H30 and H32), using the same technique described in Heap et al. (2021a). To do  
275 so, powdered offcuts of the core material were ground for 8 min with 10 ml of isopropyl alcohol  
276 in a McCrone Micronising Mill using ZrO<sub>2</sub> cylinder elements. The XRPD analyses were  
277 performed on side-loaded powder mounts using a Bruker D8 Advance Eco X-ray diffractometer  
278 (CuK $\alpha$ , 40 kV, 25 mA, 2–75° 2 $\theta$ , 0.01° step size, 15 mm irradiated length, 2.5° primary and  
279 secondary sollers, and a LynxEye XE-T detector). The phases in the whole rock powders were  
280 then quantified using the Rietveld program BGMN (Bergmann et al., 1998) and the Profex  
281 graphical user interface (Döbelin and Kleeberg, 2015). To identify clay minerals, < 2  $\mu$ m  
282 fractions were separated by gravitational settling, and oriented mounts were X-rayed in an air-  
283 dried state, an ethylene-glycolated state, and following exposure to 550 °C. Selected mineral  
284 phases were additionally identified by micro-Raman spectroscopy using a Horiba Jobin Yvon  
285 XploRA PLUS confocal Raman microscope. The spectrometer was equipped with a frequency-  
286 double Nd:YAG laser (532 nm, with a maximum power of 22.5 mW) and an Olympus  
287 LMPLFLN 100 $\times$  long-working-distance objective with a numerical aperture of 0.9.

288

## 289 **4 Results**

### 290 4.1 Microstructure, mineralogy, and alteration

291 The mineral contents for each of the 19 rock blocks from the main sample suite (“H”  
292 series) are available in Table 1 (data for all but samples H30 and H32 were presented in Heap  
293 et al., 2021a). All of the andesite blocks are characterised by a porphyritic texture comprising

294 phenocrysts (often a few hundred microns long, but occasionally as large as 1–2 mm) of  
 295 dominantly plagioclase and pyroxene (orthopyroxene and clinopyroxene) within a crystallised  
 296 groundmass (Figures 3 and 4; Heap et al., 2021a). Microcracks and pores (with a diameter  
 297 ranging from a couple of tens of microns to almost 1 mm) are present in all of the samples  
 298 (Figures 3 and 4; Heap et al., 2021a).

299 All of the samples also contain variable quantities of secondary minerals, including  
 300 kaolinite, alunite or natro-alunite, silica polymorphs (quartz, cristobalite, tridymite, and opal-  
 301 A), hematite, pyrite, gypsum, and talc (secondary minerals are indicated by asterisks in Table  
 302 1). The most abundant secondary minerals are kaolinite, natro-alunite, and cristobalite (Table  
 303 1). Kaolinite is present as a replacement mineral in altered plagioclases and as a microcrack-  
 304 and pore-filling precipitate, and natro-alunite and cristobalite are present as microcrack- and  
 305 pore-filling precipitates (Figures 3 and 4). The observed secondary mineral assemblage  
 306 corresponds to intermediate to advanced argillic alteration (Heap et al., 2021a).

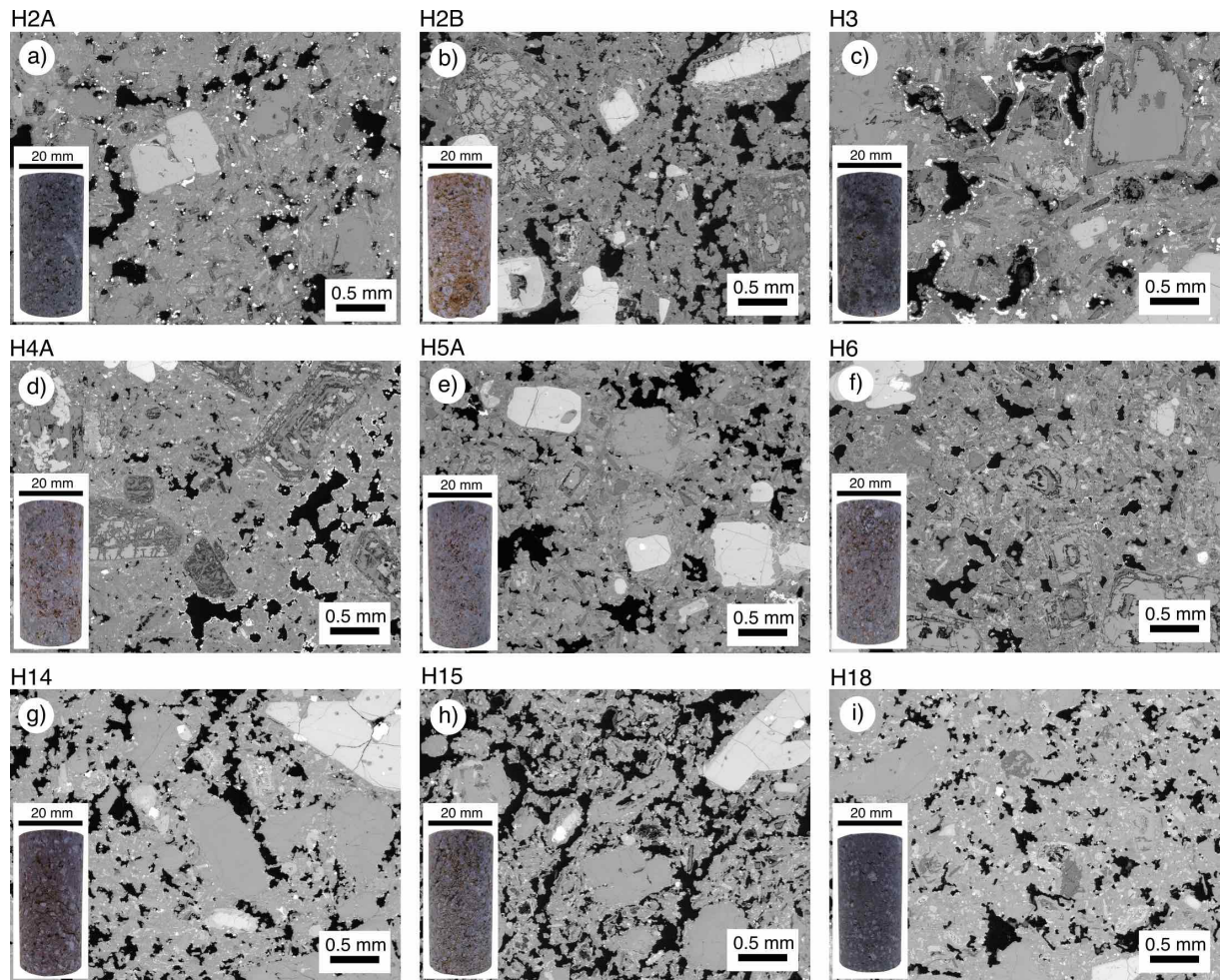
307 Based on the results of the XRPD, each of the 19 rock blocks from the “H” series are  
 308 assigned a value of alteration—the weight percentage of secondary minerals in the block—  
 309 which ranges from 6 wt.% (sample H32) up to 85.4 wt.% (sample H30) (Table 2).

310

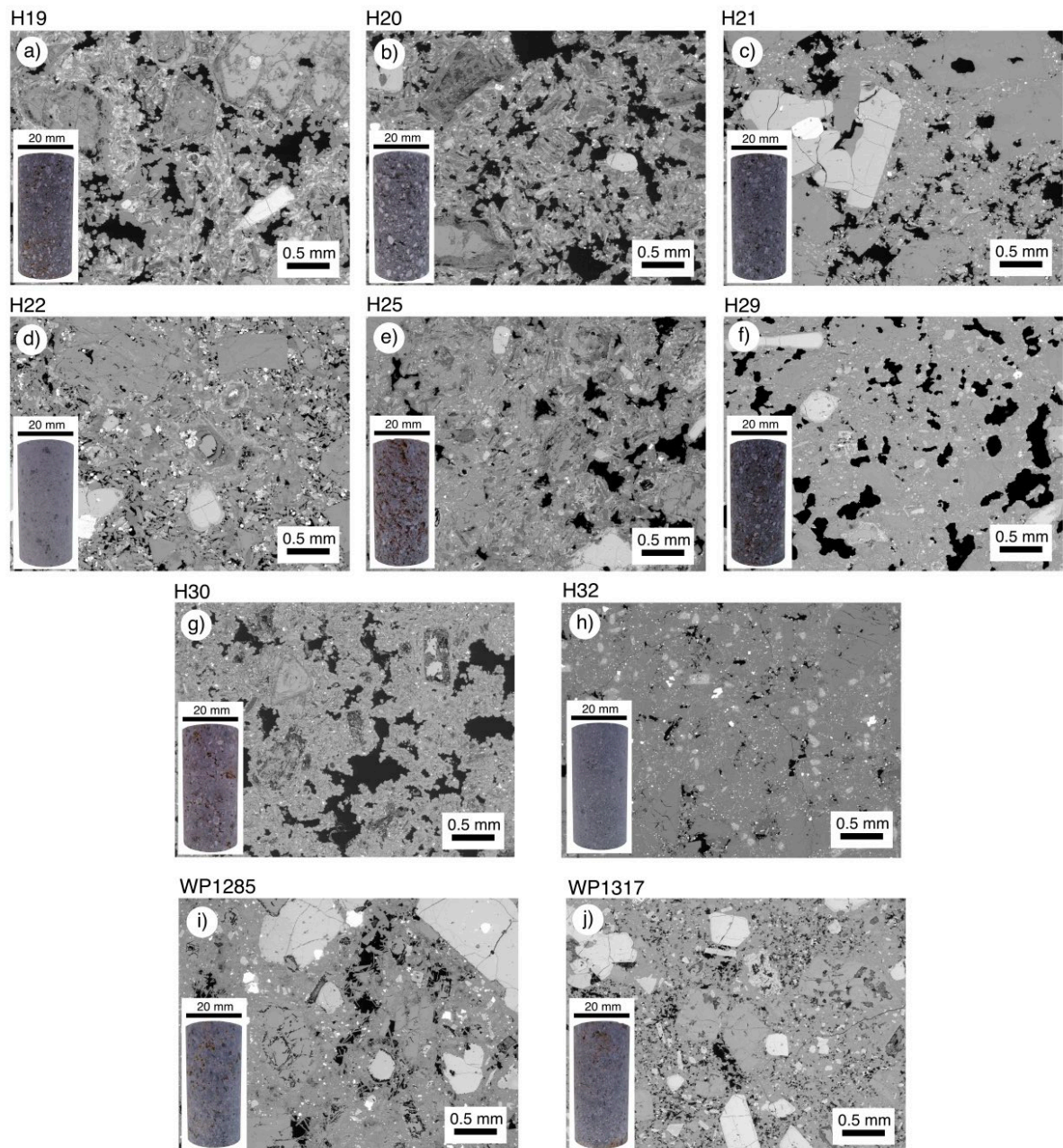
Mineral	H2 A	H2 B	H3	H4 A	H5 A	H6	H1 4	H1 5	H1 8	H1 9	H2 0	H2 1	H2 2	H2 5	H2 9	H3 0	H3 2	WP128 5	WP131 7
Plagioclase	56.7	12.3	46.6	23.3	41.3	30.0	60.7	22.5	61.2	22.0	28.7	24.2	59.5	38.7	62.4	8.9	64.4	64.7	61.6
Clinopyroxene	8.7	3.4	5.6	4.9	5.2	6.4	6.3	7.3	8.4	5.0	8.9	12.4	8.9	5.3	7.8	2.5	9.5	5.2	5.9
Orthopyroxene	10.8	9.5	11.8	11.8	11.1	10.8	8.6	9.2	12.2	10.2	15.0	19.3	13.6	10.2	11.2	3.3	15.1	13.2	15.6
(Ti-) Magnetite	0.7	-	0.8	-	-	-	0.8	-	2.9	-	2.4	3.1	0.8	-	2.7	-	4.9	3.5	0.7
Quartz*	1.0	0.5	0.6	0.6	0.5	0.5	1.7	0.7	0.7	1.7	0.3	0.2	0.6	0.3	0.4	0.9	0.3	0.2	0.7
Cristobalite*	11.3	12.8	10.6	11.8	13.0	11.1	13.5	10.2	11.7	9.5	11.4	11.7	10.6	9.8	12.4	9	5.7	-	-
Tridymite*	-	-	-	-	-	-	-	0.7	-	-	-	-	-	-	-	-	-	13.2	13.2
Hematite*	-	-	-	-	-	-	3.4	-	2.8	2.4	-	-	-	-	3.1	4.3	-	-	-
Pyrite*	3.5	-	3.8	2.3	-	-	-	-	-	-	-	0.4	3.1	0.6	-	-	-	-	-
Alunite*	-	-	-	-	-	-	-	-	-	-	-	-	-	-	-	-	-	-	2.4
Na-Alunite*	1.4	1.6	2.8	1.3	5.4	5.1	5.1	15.0	-	14.2	0.5	0.5	-	9.8	-	25.6	-	-	-
Gypsum*	-	-	-	0.7	-	-	-	-	-	-	0.8	1.2	-	-	-	-	-	-	-
Kaolinite*	6	59.7	17.4	43.3	23.5	36.0	<1	34.3	-	2.0	2.0	2.0	<1	25.3	-	35.6	-	-	
Talc*	-	-	-	-	-	-	-	-	-	-	-	-	2.9	-	-	-	-	-	-
Opal-A*	-	-	-	-	-	-	-	-	33.0	30.0	25.0	-	-	-	10.0	10	-	-	-

311

312 **Table 1.** Mineral contents, measured by X-ray powder diffraction, of the 19 rock blocks from  
313 the main sample suite (“H” series). Values in wt.%. Asterisk denotes a secondary mineral (i.e.  
314 alteration mineral). All data, except those for H30 and H32, were taken from Heap et al.  
315 (2021a).  
316



317  
318 **Figure 3.** Backscattered scanning electron microscope images of andesites from La Soufrière  
319 de Guadeloupe (Eastern Caribbean). Insets show a photograph of 20 mm-diameter sample  
320 prepared from the block. (a) H2A. (b) H2B. (c) H3. (d) H4A. (e) H5A. (f) H6. (g) H14. (h)  
321 H15. (i) H18.  
322



323

324 **Figure 4.** Backscattered scanning electron microscope images of andesites from La Soufrière

325 de Guadeloupe (Eastern Caribbean). Insets show a photograph of 20 mm-diameter sample

326 prepared from the block. (a) H19. (b) H20. (c) H21. (d) H22. (e) H25. (f) H29. (g) H30. (h)

327

H32. (i) WP1285. (j) WP1317.

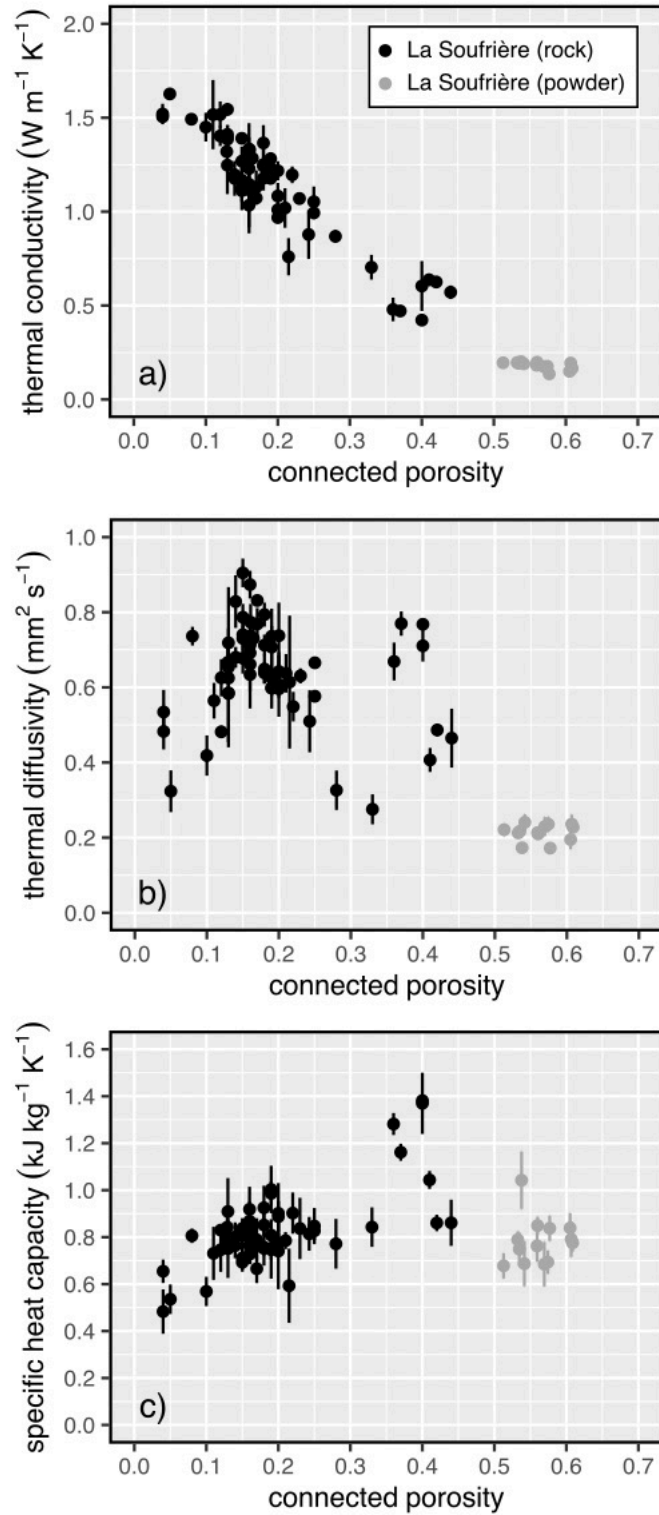
328

329 4.2 Thermal properties

330 Thermal conductivity, thermal diffusivity, and specific heat capacity for all the samples  
331 (rocks and powders) are plotted as a function of porosity in Figure 5 (data available in Table  
332 2). If we consider both types of sample (rocks and powders), we find that thermal conductivity  
333 and thermal diffusivity decrease as a function of porosity, and that specific heat capacity does  
334 not change systematically as a function of porosity (Figure 5). The trend with increasing  
335 porosity is much more evident in the thermal conductivity data (Figure 5a) than in the thermal  
336 diffusivity data (Figure 5b).

337 The porosity of the rock samples varies from 0.04 to 0.44, and the porosity of the  
338 powders during the measurements, compacted using a 1 kg weight, varies between 0.51 and  
339 0.61. For the rock samples, thermal conductivity decreases from  $\sim 1.6 \text{ W}\cdot\text{m}^{-1}\cdot\text{K}^{-1}$  at a porosity  
340 of  $\sim 0.04$  to  $\sim 0.5 \text{ W}\cdot\text{m}^{-1}\cdot\text{K}^{-1}$  at a porosity of  $\sim 0.4$  (Figure 5a). The thermal conductivity of the  
341 powder samples is  $\sim 0.2 \text{ W}\cdot\text{m}^{-1}\cdot\text{K}^{-1}$  for all samples (Figure 5a). The thermal diffusivity of the  
342 rock samples generally decreases from  $\sim 0.9$  to  $\sim 0.3 \text{ mm}^2\cdot\text{s}^{-1}$  as porosity increases, and the  
343 thermal diffusivity of the powder samples is  $\sim 0.22 \text{ mm}^2\cdot\text{s}^{-1}$  for all samples (Figure 5b).  
344 Excluding a few outliers, the specific heat capacity is  $\sim 0.8 \text{ kJ}\cdot\text{kg}^{-1}\cdot\text{K}^{-1}$  for all samples (rocks  
345 and powders), regardless of their porosity (Figure 5c).

346



347

348 **Figure 5.** Thermal conductivity, thermal diffusivity, and specific heat capacity as a function

349 of connected porosity for the rocks (black symbols) and unlithified materials (powders; grey

350 symbols) from La Soufrière de Guadeloupe (Eastern Caribbean).

351

sample number	sample type	connected porosity	weight percentage of secondary minerals	thermal conductivity ( $\text{W}\cdot\text{m}^{-1}\cdot\text{K}^{-1}$ )	thermal diffusivity ( $\text{mm}^2\cdot\text{s}^{-1}$ )	specific heat capacity ( $\text{kJ}\cdot\text{kg}^{-1}\cdot\text{K}^{-1}$ )
H2A	rock	0.18	23.2	$1.37 \pm 0.10$	$0.79 \pm 0.03$	$0.75 \pm 0.03$
H2A	rock	0.19	23.2	$1.23 \pm 0.08$	$0.74 \pm 0.07$	$0.75 \pm 0.13$
H2A	rock	0.20	23.2	$1.01 \pm 0.04$	$0.60 \pm 0.02$	$0.77 \pm 0.04$
H2B	rock	0.42	74.6	$0.63 \pm 0.02$	$0.49 \pm 0.02$	$0.86 \pm 0.04$
H2B	rock	0.44	74.6	$0.57 \pm 0.04$	$0.46 \pm 0.08$	$0.86 \pm 0.10$
H2B	rock	0.41	74.6	$0.64 \pm 0.03$	$0.41 \pm 0.03$	$1.04 \pm 0.04$
H3	rock	0.19	35.2	$1.28 \pm 0.03$	$0.62 \pm 0.04$	$0.99 \pm 0.05$
H3	rock	0.16	35.2	$1.33 \pm 0.06$	$0.69 \pm 0.10$	$0.87 \pm 0.15$
H3	rock	0.15	35.2	$1.39 \pm 0.03$	$0.73 \pm 0.01$	$0.84 \pm 0.02$
H4A	rock	0.23	60.0	$1.07 \pm 0.03$	$0.63 \pm 0.02$	$0.84 \pm 0.13$
H4A	rock	0.25	60.0	$0.99 \pm 0.03$	$0.67 \pm 0.01$	$0.85 \pm 0.08$
H4A	rock	0.20	60.0	$1.08 \pm 0.07$	$0.64 \pm 0.04$	$0.89 \pm 0.07$
H5A	rock	0.16	42.4	$1.28 \pm 0.06$	$0.66 \pm 0.03$	$0.80 \pm 0.03$
H5A	rock	0.18	42.4	$1.25 \pm 0.02$	$0.64 \pm 0.03$	$0.85 \pm 0.05$
H5A	rock	0.15	42.4	$1.27 \pm 0.08$	$0.68 \pm 0.04$	$0.82 \pm 0.05$
H6	rock	0.18	52.7	$1.18 \pm 0.02$	$0.65 \pm 0.04$	$0.93 \pm 0.09$
H6	rock	0.19	52.7	$1.18 \pm 0.02$	$0.60 \pm 0.06$	$1.00 \pm 0.10$
H6	rock	0.16	52.7	$1.23 \pm 0.02$	$0.71 \pm 0.05$	$0.82 \pm 0.08$
H14	rock	0.19	23.7	$1.20 \pm 0.03$	$0.71 \pm 0.06$	$0.75 \pm 0.04$
H14	rock	0.20	23.7	$1.22 \pm 0.05$	$0.61 \pm 0.09$	$0.90 \pm 0.13$
H14	rock	0.18	23.7	$1.24 \pm 0.13$	$0.71 \pm 0.03$	$0.76 \pm 0.08$
H15	rock	0.28	60.9	$0.87 \pm 0.03$	$0.33 \pm 0.05$	$0.77 \pm 0.11$
H15	rock	0.33	60.9	$0.70 \pm 0.07$	$0.28 \pm 0.04$	$0.84 \pm 0.08$
H18	rock	0.13	15.2	$1.39 \pm 0.08$	$0.59 \pm 0.02$	$0.80 \pm 0.05$
H18	rock	0.13	15.2	$1.41 \pm 0.05$	$0.65 \pm 0.21$	$0.79 \pm 0.05$
H18	rock	0.12	15.2	$1.40 \pm 0.05$	$0.48 \pm 0.02$	$0.83 \pm 0.02$
H19	rock	0.15	62.8	$1.13 \pm 0.04$	$0.74 \pm 0.04$	$0.69 \pm 0.03$
H19	rock	0.17	62.8	$1.07 \pm 0.04$	$0.77 \pm 0.04$	$0.67 \pm 0.06$
H19	rock	0.20	62.8	$0.97 \pm 0.03$	$0.74 \pm 0.09$	$0.74 \pm 0.16$
H20	rock	0.37	45.0	$0.47 \pm 0.03$	$0.77 \pm 0.03$	$1.16 \pm 0.04$
H20	rock	0.36	45.0	$0.48 \pm 0.06$	$0.67 \pm 0.05$	$1.28 \pm 0.05$
H20	rock	0.40	45.0	$0.42 \pm 0.02$	$0.71 \pm 0.04$	$1.37 \pm 0.13$
H21	rock	0.15	41.0	$1.17 \pm 0.12$	$0.90 \pm 0.04$	$0.71 \pm 0.06$
H21	rock	0.17	41.0	$1.13 \pm 0.09$	$0.83 \pm 0.01$	$0.79 \pm 0.09$
H21	rock	0.16	41.0	$1.12 \pm 0.20$	$0.87 \pm 0.04$	$0.77 \pm 0.04$
H22	rock	0.12	17.2	$1.52 \pm 0.07$	$0.63 \pm 0.05$	$0.75 \pm 0.09$
H22	rock	0.11	17.2	$1.52 \pm 0.18$	$0.56 \pm 0.05$	$0.73 \pm 0.11$
H22	rock	0.13	17.2	$1.54 \pm 0.03$	$0.62 \pm 0.02$	$0.77 \pm 0.03$
H25	rock	0.16	45.8	$1.15 \pm 0.07$	$0.63 \pm 0.09$	$0.85 \pm 0.10$
H25	rock	0.21	45.8	$1.02 \pm 0.11$	$0.64 \pm 0.05$	$0.79 \pm 0.04$
H25	rock	0.14	45.8	$1.20 \pm 0.03$	$0.68 \pm 0.03$	$0.76 \pm 0.05$
H29	rock	0.22	25.9	$1.20 \pm 0.04$	$0.55 \pm 0.04$	$0.90 \pm 0.09$
H29	rock	0.25	25.9	$1.05 \pm 0.08$	$0.58 \pm 0.02$	$0.83 \pm 0.04$
H29	rock	0.19	25.9	$1.20 \pm 0.04$	$0.60 \pm 0.02$	$0.81 \pm 0.06$

H30	rock	0.16	85.4	1.30 ± 0.17	0.74 ± 0.01	0.92 ± 0.01
H30	rock	0.40	85.4	0.60 ± 0.13	0.77 ± 0.01	1.38 ± 0.02
H32	rock	0.04	6.0	1.52 ± 0.05	0.48 ± 0.05	0.65 ± 0.05
H32	rock	0.04	6.0	1.51 ± 0.01	0.53 ± 0.06	0.48 ± 0.09
H32	rock	0.05	6.0	1.63 ± 0.01	0.32 ± 0.06	0.54 ± 0.06
WP1317	rock	0.16	16.3	1.03 ± 0.15	0.73 ± 0.03	0.85 ± 0.05
WP1317	rock	0.15	16.3	1.11 ± 0.10	0.79 ± 0.04	0.81 ± 0.07
WP1317	rock	0.14	16.3	1.18 ± 0.09	0.83 ± 0.07	0.80 ± 0.06
WP1285	rock	0.13	13.4	1.40 ± 0.02	0.72 ± 0.04	0.75 ± 0.12
WP1285	rock	0.10	13.4	1.45 ± 0.08	0.42 ± 0.05	0.57 ± 0.06
WP1285	rock	0.08	13.4	1.49 ± 0.01	0.74 ± 0.02	0.81 ± 0.03
SAM58	rock	0.14	-	1.18 ± 0.02	0.66 ± 0.03	0.75 ± 0.05
SAM58	rock	0.14	-	1.21 ± 0.05	0.65 ± 0.03	0.78 ± 0.04
S005	rock	0.22	-	0.76 ± 0.10	0.61 ± 0.18	0.59 ± 0.16
S005	rock	0.24	-	0.88 ± 0.13	0.51 ± 0.08	0.81 ± 0.07
S008	rock	0.17	-	1.28 ± 0.04	0.73 ± 0.03	0.75 ± 0.02
S008	rock	0.16	-	1.33 ± 0.02	0.77 ± 0.05	0.73 ± 0.04
S016	rock	0.13	-	1.32 ± 0.03	0.67 ± 0.05	0.84 ± 0.06
S016	rock	0.13	-	1.25 ± 0.15	0.58 ± 0.13	0.91 ± 0.14
S001	powder	0.61	-	0.19 ± 0.00	0.24 ± 0.02	0.79 ± 0.08
S002	powder	0.56	-	0.20 ± 0.01	0.21 ± 0.01	0.85 ± 0.04
S003	powder	0.53	-	0.20 ± 0.01	0.21 ± 0.00	0.79 ± 0.03
S004	powder	0.61	-	0.15 ± 0.01	0.19 ± 0.03	0.84 ± 0.06
S006	powder	0.57	-	0.18 ± 0.01	0.23 ± 0.03	0.68 ± 0.09
S007	powder	0.56	-	0.18 ± 0.01	0.21 ± 0.02	0.76 ± 0.07
S009	powder	0.51	-	0.20 ± 0.01	0.22 ± 0.02	0.68 ± 0.05
S010	powder	0.54	-	0.19 ± 0.01	0.22 ± 0.01	0.75 ± 0.07
S011	powder	0.57	-	0.18 ± 0.00	0.24 ± 0.02	0.69 ± 0.05
S012	powder	0.61	-	0.17 ± 0.01	0.23 ± 0.01	0.78 ± 0.04
S013	powder	0.54	-	0.19 ± 0.01	0.24 ± 0.02	0.69 ± 0.10
S014	powder	0.58	-	0.14 ± 0.00	0.17 ± 0.01	0.84 ± 0.05
S015	powder	0.54	-	0.20 ± 0.02	0.17 ± 0.01	1.04 ± 0.12

352

353 **Table 2.** Connected porosity, weight percentage of secondary minerals, thermal conductivity,  
354 thermal diffusivity, and specific heat capacity for the samples from La Soufrière de  
355 Guadeloupe (Eastern Caribbean) measured for this study. The standard deviations provided  
356 relate to measurement precision (calculated using the four measurements). The standard  
357 uncertainty for values of thermal conductivity and thermal diffusivity using the transient hot-  
358 strip method has been determined to be 2.6 and 11%, respectively (Hammerschmidt and  
359 Sabuga, 2000).

volcano	rock type	connected porosity	weight percentage of secondary minerals	thermal conductivity ( $\text{W}\cdot\text{m}^{-1}\cdot\text{K}^{-1}$ )	thermal diffusivity ( $\text{mm}^2\cdot\text{s}^{-1}$ )	specific heat capacity ( $\text{kJ}\cdot\text{kg}^{-1}\cdot\text{K}^{-1}$ )
Chaos Crags	rhyodacite	0.153	6.4	$1.14 \pm 0.03$	$0.65 \pm 0.02$	$0.78 \pm 0.02$
Chaos Crags	rhyodacite	0.139	14.6	$1.29 \pm 0.03$	$0.73 \pm 0.07$	$0.78 \pm 0.08$
Chaos Crags	rhyodacite	0.125	14.6	$1.52 \pm 0.26$	$0.84 \pm 0.09$	$0.77 \pm 0.07$
Chaos Crags	rhyodacite	0.138	14.6	$1.40 \pm 0.24$	$0.94 \pm 0.06$	$0.66 \pm 0.15$
Chaos Crags	rhyodacite	0.076	16.5	$1.66 \pm 0.09$	$0.89 \pm 0.07$	$0.77 \pm 0.02$
Chaos Crags	rhyodacite	0.142	16.5	$1.51 \pm 0.28$	$0.90 \pm 0.13$	$0.72 \pm 0.05$
Chaos Crags	rhyodacite	0.115	16.5	$1.44 \pm 0.17$	$0.78 \pm 0.11$	$0.78 \pm 0.03$
Merapi	basaltic-andesite	0.080	7.5	$1.43 \pm 0.02$	$0.70 \pm 0.04$	$0.79 \pm 0.03$
Merapi	basaltic-andesite	0.084	7.5	$1.37 \pm 0.03$	$0.73 \pm 0.03$	$0.74 \pm 0.02$
Merapi	basaltic-andesite	0.077	7.5	$1.48 \pm 0.02$	$0.73 \pm 0.04$	$0.79 \pm 0.04$
Merapi	basaltic-andesite	0.079	29.0	$1.20 \pm 0.02$	$0.57 \pm 0.02$	$0.86 \pm 0.04$
Merapi	basaltic-andesite	0.080	29.0	$1.23 \pm 0.05$	$0.57 \pm 0.03$	$0.87 \pm 0.02$
Merapi	basaltic-andesite	0.083	29.0	$1.28 \pm 0.01$	$0.53 \pm 0.02$	$0.98 \pm 0.03$
Merapi	basaltic-andesite	0.154	45.0	$1.06 \pm 0.07$	$0.51 \pm 0.03$	$0.90 \pm 0.04$
Merapi	basaltic-andesite	0.182	45.0	$0.90 \pm 0.06$	$0.51 \pm 0.03$	$0.81 \pm 0.01$
Merapi	basaltic-andesite	0.144	45.0	$1.07 \pm 0.05$	$0.53 \pm 0.01$	$0.91 \pm 0.06$
Merapi	basaltic-andesite	0.155	45.0	$1.04 \pm 0.01$	$0.52 \pm 0.02$	$0.88 \pm 0.04$
Merapi	basaltic-andesite	0.160	45.0	$0.97 \pm 0.08$	$0.54 \pm 0.03$	$0.81 \pm 0.06$
Merapi	basaltic-andesite	0.162	45.0	$0.97 \pm 0.01$	$0.66 \pm 0.21$	$0.73 \pm 0.23$
Merapi	basaltic-andesite	0.182	45.0	$0.94 \pm 0.00$	$0.43 \pm 0.00$	$0.99 \pm 0.00$
Merapi	basaltic-andesite	0.215	62.0	$0.78 \pm 0.08$	$0.60 \pm 0.09$	$0.66 \pm 0.18$
Merapi	basaltic-andesite	0.233	62.0	$0.80 \pm 0.04$	$0.51 \pm 0.09$	$0.79 \pm 0.10$
Merapi	basaltic-andesite	0.220	62.0	$0.86 \pm 0.07$	$0.51 \pm 0.04$	$0.82 \pm 0.02$
Merapi	basaltic-andesite	0.188	62.0	$0.86 \pm 0.06$	$0.50 \pm 0.03$	$0.82 \pm 0.02$
Merapi	basaltic-andesite	0.163	62.0	$0.88 \pm 0.01$	$0.55 \pm 0.04$	$0.75 \pm 0.06$
Merapi	basaltic-andesite	0.242	62.0	$0.79 \pm 0.05$	$0.46 \pm 0.00$	$0.86 \pm 0.05$
Merapi	basaltic-andesite	0.263	62.0	$0.79 \pm 0.01$	$0.47 \pm 0.04$	$0.88 \pm 0.07$
Merapi	basaltic-andesite	0.168	62.0	$0.85 \pm 0.03$	$0.44 \pm 0.09$	$0.92 \pm 0.19$
Merapi	basaltic-andesite	0.231	32.5	$0.75 \pm 0.06$	$0.45 \pm 0.06$	$0.80 \pm 0.11$
Merapi	basaltic-andesite	0.236	32.5	$0.76 \pm 0.05$	$0.51 \pm 0.02$	$0.70 \pm 0.07$
Merapi	basaltic-andesite	0.262	32.5	$0.76 \pm 0.04$	$0.55 \pm 0.11$	$0.70 \pm 0.11$
Merapi	basaltic-andesite	0.256	32.5	$0.75 \pm 0.05$	$0.47 \pm 0.05$	$0.78 \pm 0.06$
Ruapehu	andesite	0.021	-	$1.54 \pm 0.02$	$0.70 \pm 0.02$	$0.80 \pm 0.03$
Ruapehu	andesite	0.040	-	$1.62 \pm 0.02$	$0.77 \pm 0.02$	$0.78 \pm 0.01$
Ruapehu	andesite	0.024	-	$1.47 \pm 0.06$	$0.77 \pm 0.07$	$0.72 \pm 0.10$
Ruapehu	andesite	0.036	-	$1.46 \pm 0.05$	$0.75 \pm 0.01$	$0.73 \pm 0.02$
Ruapehu	andesite	0.042	-	$1.53 \pm 0.01$	$0.76 \pm 0.03$	$0.74 \pm 0.04$
Ruapehu	andesite	0.047	-	$1.51 \pm 0.05$	$0.72 \pm 0.05$	$0.79 \pm 0.09$
Ruapehu	andesite	0.038	-	$1.45 \pm 0.03$	$0.70 \pm 0.03$	$0.77 \pm 0.05$
Ruapehu	andesite	0.036	-	$1.50 \pm 0.00$	$0.72 \pm 0.01$	$0.78 \pm 0.01$
Ruapehu	andesite	0.024	-	$1.48 \pm 0.02$	$0.71 \pm 0.02$	$0.77 \pm 0.03$
Ruapehu	andesite	0.027	-	$1.46 \pm 0.03$	$0.68 \pm 0.01$	$0.79 \pm 0.00$
Ruapehu	andesite	0.048	-	$1.39 \pm 0.01$	$0.83 \pm 0.06$	$0.64 \pm 0.04$
Ruapehu	andesite	0.042	-	$1.41 \pm 0.00$	$0.66 \pm 0.00$	$0.80 \pm 0.00$
Ruapehu	andesite	0.184	-	$1.06 \pm 0.01$	$0.65 \pm 0.04$	$0.73 \pm 0.05$
Ruapehu	andesite	0.205	-	$1.00 \pm 0.05$	$0.58 \pm 0.05$	$0.79 \pm 0.11$
Ruapehu	andesite	0.098	-	$1.26 \pm 0.01$	$0.70 \pm 0.04$	$0.72 \pm 0.04$
Ruapehu	andesite	0.118	-	$1.22 \pm 0.06$	$0.65 \pm 0.05$	$0.77 \pm 0.10$

Ruapehu	andesite	0.153	-	$1.16 \pm 0.05$	$0.66 \pm 0.08$	$0.75 \pm 0.06$
Ruapehu	andesite	0.140	-	$1.23 \pm 0.05$	$0.71 \pm 0.06$	$0.73 \pm 0.08$
Ruapehu	andesite	0.149	-	$1.14 \pm 0.04$	$0.65 \pm 0.02$	$0.73 \pm 0.05$
Ruapehu	andesite	0.167	-	$1.08 \pm 0.09$	$0.72 \pm 0.09$	$0.65 \pm 0.03$
Ruapehu	andesite	0.129	-	$1.21 \pm 0.04$	$0.59 \pm 0.01$	$0.86 \pm 0.04$
Ruapehu	andesite	0.151	-	$1.13 \pm 0.05$	$0.60 \pm 0.06$	$0.80 \pm 0.05$
Ruapehu	andesite	0.204	-	$1.01 \pm 0.05$	$0.61 \pm 0.03$	$0.75 \pm 0.00$
Ruapehu	andesite	0.182	-	$1.09 \pm 0.02$	$0.62 \pm 0.05$	$0.78 \pm 0.05$
Ruapehu	andesite	0.308	-	$0.81 \pm 0.00$	$0.64 \pm 0.03$	$0.66 \pm 0.03$
Ruapehu	andesite	0.320	-	$0.84 \pm 0.00$	$0.75 \pm 0.11$	$0.61 \pm 0.10$
Ruapehu	andesite	0.345	-	$0.81 \pm 0.04$	$0.52 \pm 0.05$	$0.85 \pm 0.05$
Ruapehu	andesite	0.348	-	$0.81 \pm 0.06$	$0.59 \pm 0.02$	$0.76 \pm 0.05$
Ruapehu	andesite	0.333	-	$0.79 \pm 0.05$	$0.53 \pm 0.06$	$0.81 \pm 0.07$
Ruapehu	andesite	0.382	-	$0.72 \pm 0.04$	$0.63 \pm 0.09$	$0.68 \pm 0.14$
Ruapehu	andesite	0.602	-	$0.43 \pm 0.03$	$0.51 \pm 0.04$	$0.79 \pm 0.02$
Ruapehu	andesite	0.628	-	$0.38 \pm 0.03$	$0.55 \pm 0.08$	$0.71 \pm 0.16$

361

362 **Table 3.** Connected porosity, weight percentage of secondary minerals, thermal conductivity,  
363 thermal diffusivity, and specific heat capacity for the samples from Chaos Crags (USA; data  
364 unique to this study), Merapi volcano (Indonesia; data from Heap et al., 2020a), and Ruapehu  
365 (New Zealand; data from Heap et al, 2020a). All of the samples listed are rock samples.

366 Alteration (percentage of secondary minerals) of the samples from Merapi volcano was not  
367 reported in Heap et al. (2020a). XRPD data are not available for the samples from Ruapehu  
368 and so alteration values are not reported. The standard deviations provided relate to  
369 measurement precision (calculated using the four measurements). The standard uncertainty  
370 for values of thermal conductivity and thermal diffusivity using the transient hot-strip method  
371 has been determined to be 2.6 and 11%, respectively (Hammerschmidt and Sabuga, 2000).

372

## 373 **5 Discussion**

### 374 5.1 The influence of porosity on thermal properties

375 To better understand the influence of porosity on the thermal properties of volcanic  
376 rocks, we compare our new data for rocks and powders La Soufrière (Table 2) with published  
377 data from Heap et al. (2020a) for rocks from Ruapehu and Merapi volcano (Table 3) and new  
378 data for variably-altered rhyodacites from Chaos Crags (Lassen Volcanic National Park,

379 California, USA) (Table 3). The blocks from Ruapehu are variably porous (from <0.05 to ~0.6)  
380 and relatively unaltered porphyritic andesites that contain large phenocrysts of plagioclase and  
381 pyroxene within a glassy microlite-rich groundmass (Heap and Kennedy, 2016; Heap et al.,  
382 2020a). The blocks from Merapi volcano are variably altered basaltic-andesites with porphyritic  
383 texture comprising phenocrysts of dominantly plagioclase and pyroxene within a crystallised  
384 groundmass (Heap et al., 2019, 2020a). The alteration phases present are similar to those found  
385 in the blocks from La Soufrière, and include natro-alunite, alunite, quartz, hematite, cristobalite,  
386 gypsum, and unclassified amorphous phases (Heap et al., 2019, 2020a). The alteration of the  
387 blocks from Merapi volcano—the percentage of secondary minerals in the block—ranges from  
388 7.5 wt.% up to 62 wt.% (Table 3). The blocks from Chaos Crags, described in Ryan et al. (2020)  
389 and Heap et al. (2021b), are porphyritic rhyodacites containing phenocrysts of dominantly  
390 plagioclase, K-feldspar, and quartz within a crystallised groundmass. Secondary minerals  
391 include cristobalite, hematite, smectite, and kaolinite (Heap et al., 2021b). The alteration of the  
392 rhyodacite blocks from Chaos Crags ranges from 6.4 wt.% up to 16.5 wt.% (Table 3). The  
393 thermal properties of cylindrical samples prepared from these blocks (Ruapehu, Merapi  
394 volcano, and Chaos Crags) were measured using the same Hot Disk® Thermal Constants  
395 Analyser used to measure the samples from La Soufrière, as described above, adding  
396 confidence to direct data comparisons.

397 The effective thermal conductivity,  $\lambda(\phi)$ , can be determined using the Maxwell result  
398 for conduction in a porous medium,

399

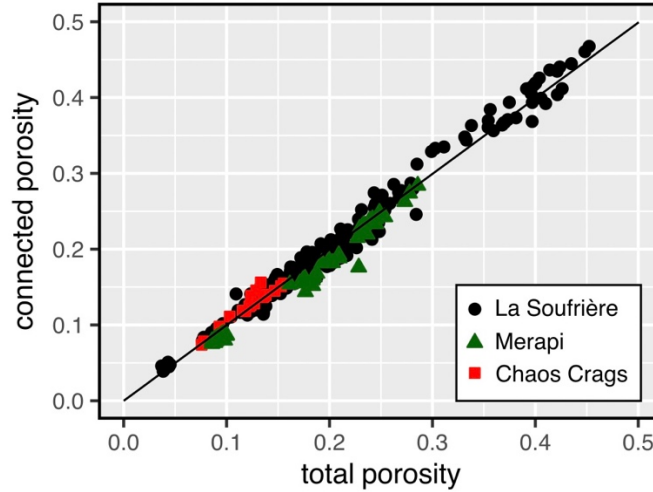
$$400 \quad \frac{\lambda(\phi)}{\lambda_0} = \frac{(1 - \phi)(1 - r) + r\beta\phi}{(1 - \phi)(1 - r) + \beta\phi}, (1)$$

401

402 where  $\phi$  is the total porosity,  $r = \lambda_f/\lambda_0$  (where  $\lambda_f$  and  $\lambda_0$  are the thermal conductivities of  
403 the pore-filling fluid and the rock groundmass, respectively; Zimmerman, 1989). We assume

404 spherical pores, and so  $\beta = 3(1 - r)/(2 + r)$  (Zimmerman, 1989). The Maxwell model is a  
405 dilute approximation and so assumes no interaction between the spherical pores. Because our  
406 thermal conductivity data are for dry materials, we assume a pore fluid thermal conductivity,  
407  $\lambda_f$ , of  $0 \text{ W}\cdot\text{m}^{-1}\cdot\text{K}^{-1}$  (i.e. we assume that the conduction of the porosity-filling air is negligible).  
408 The Maxwell model for the effect of pores (or any inclusion) on the thermal properties of a  
409 medium (Equation (1)) is a dilute approximation for spherical pores or inclusions. By contrast,  
410 powders are the effective geometric inverse of spherical pores of gas in a continuum matrix,  
411 and are instead discrete (sub-angular or sub-spherical) particles in a continuum gas. Therefore,  
412 not only does the Maxwell model (Equation (1)) not apply, but it also is reasonable to expect  
413 that the functional form of the appropriate model for powders is different. This is explicitly  
414 documented in Torquato and Haslach (2002), who gives a range of effective medium models  
415 for the physical properties of inclusions of one phase in another phase, as well as the inverse  
416 case. As an applied example, Vasseur et al. (2016) found that the elastic properties of coherent  
417 versus powdered materials were best scaled by two different effective medium models, and that  
418 the transition from one to the other (from coherent to powdered) could be captured by a cross  
419 over between models. As a result, in the following we will only discuss the measurements  
420 performed on rock samples. Finally, we highlight that the Maxwell equation (Equation (1)), and  
421 the effective medium models below (Equations (2) and (3)), consider the total porosity, whereas  
422 we have measured the connected porosity of our samples. To assess the suitability of using  
423 these models to discuss our experimental data (Figure 5; Tables 2 and 3), we provide a plot of  
424 connected porosity as a function of total porosity for numerous 20 mm-diameter cylindrical  
425 samples from La Soufrière, Chaos Crags, and Merapi volcano (Figure 6), which shows that  
426 there is little to no isolated porosity in the studied materials.

427



428

429 **Figure 6.** Connected porosity as a function of total porosity for 20 mm-diameter cylindrical  
 430 samples from La Soufrière, Chaos Crags, and Merapi volcano. The black line shows the 1:1  
 431 line, whereat the connected porosity equals the total porosity.

432

433 We find that our data for La Soufrière, as well as data for rhyodacites from Chaos Crags  
 434 and basaltic-andesites from Merapi volcano, are bracketed by curves for which  $\lambda_0$  is 1.9 and  
 435  $0.85 \text{ W}\cdot\text{m}^{-1}\cdot\text{K}^{-1}$  (the black lines in Figure 7a). A third curve, which best captures the overall  
 436 trend of the dataset, is also provided in Figure 7a (for which  $\lambda_0$  is  $1.45 \text{ W}\cdot\text{m}^{-1}\cdot\text{K}^{-1}$ ). The  
 437 effective thermal diffusivity  $D(\phi)$  was then determined using,

438

$$439 \quad D(\phi) = \frac{\lambda(\phi)}{\rho_s C_p (1 - \phi) + \rho_f C_{p,f} \phi}, \quad (2)$$

440

441 where  $\rho_s$  and  $\rho_f$  are the groundmass and pore fluid densities, respectively, and  $C_p$  and  $C_{p,f}$  are  
 442 the groundmass and pore fluid specific heat capacity, respectively (Connor et al., 1997). We  
 443 take values of  $\rho_f$  and  $C_{p,f}$  of  $1.275 \text{ kg}\cdot\text{m}^{-3}$  and  $1.007 \text{ kJ}\cdot\text{kg}^{-1}\cdot\text{K}^{-1}$ , respectively. Values for  $\rho_s$   
 444 and  $C_p$ , guided by our data, were taken as  $2650 \text{ kg}\cdot\text{m}^{-3}$  and  $0.8 \text{ kJ}\cdot\text{kg}^{-1}\cdot\text{K}^{-1}$ , respectively.

445 Theoretical curves are provided using the  $\lambda(\phi)$  values taken from the three models shown in

446 Figure 7a (i.e.  $\lambda_0 = 1.9, 1.45, \text{ and } 0.85 \text{ W}\cdot\text{m}^{-1}\cdot\text{K}^{-1}$ ; Equation (1); the black lines in Figure 7b).  
447 Based on Equation (2), the effective specific heat capacity  $C_p(\phi)$  is given by the porosity-  
448 weighted average,

449

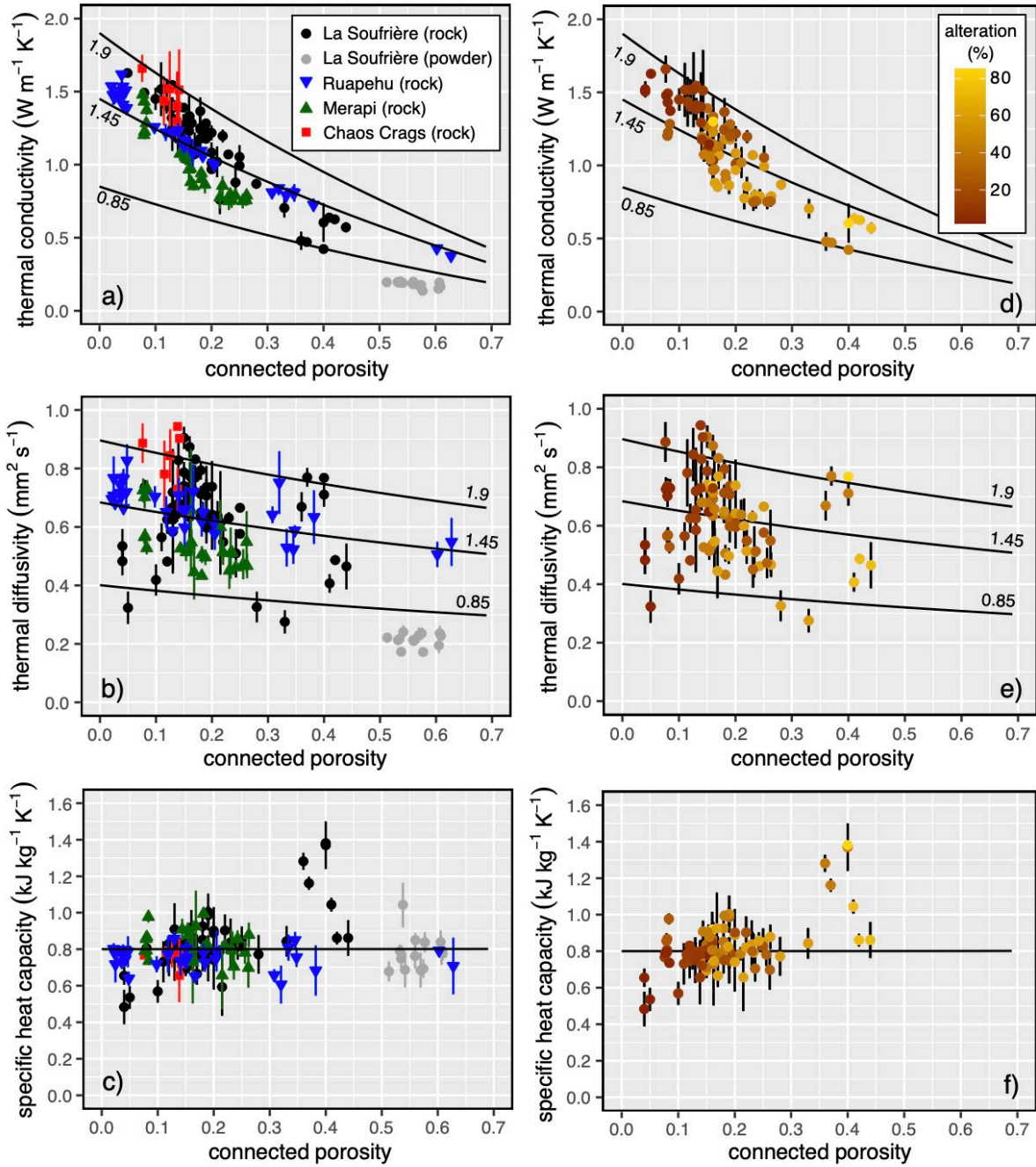
$$450 \quad C_p(\phi) = \frac{\rho_s C_p (1 - \phi) + \rho_f C_{p,f} \phi}{\rho_b}, (3)$$

451

452 where  $\rho_b$  is the bulk sample density, where  $\rho_b = \rho_s(1 - \phi) + \rho_f \phi$ . To plot  $C_p(\phi)$ , we take the  
453 same values outlined above for the different variables (the black line in Figure 7c).

454 The effective medium models (Equations (1), (2), and (3)) are in reasonable agreement  
455 with the data (Figure 7), suggesting that porosity plays an important role in governing their  
456 thermal properties (as discussed in Heap et al., 2020a). The scatter in these data, i.e. the reason  
457 why even data from the same volcano cannot be described by a single theoretical curve (Figure  
458 7), is the result of factors not considered in Equations (1), (2), and (3), such as differences in  
459 the nature of the void space (e.g., pore size, shape, and number density, microcrack density;  
460 factors that can vary significantly in volcanic rocks, see the review of Heap and Violay, 2021)  
461 and differences in their mineral componentry (e.g., variable alteration intensities and secondary  
462 mineral assemblages). The large differences in the alteration of these rocks (Tables 2 and 3),  
463 and that the effective medium approaches well describe the relatively unaltered suite of rocks  
464 from Ruapehu (Figure 7; Heap et al., 2020a) and Hawai'i (Robertson and Peck, 1974) with  
465 variable pore sizes and shapes, suggest that the scatter in the data can be explained by their  
466 variable alteration, discussed in the next section.

467



468

469

470

471

472

473

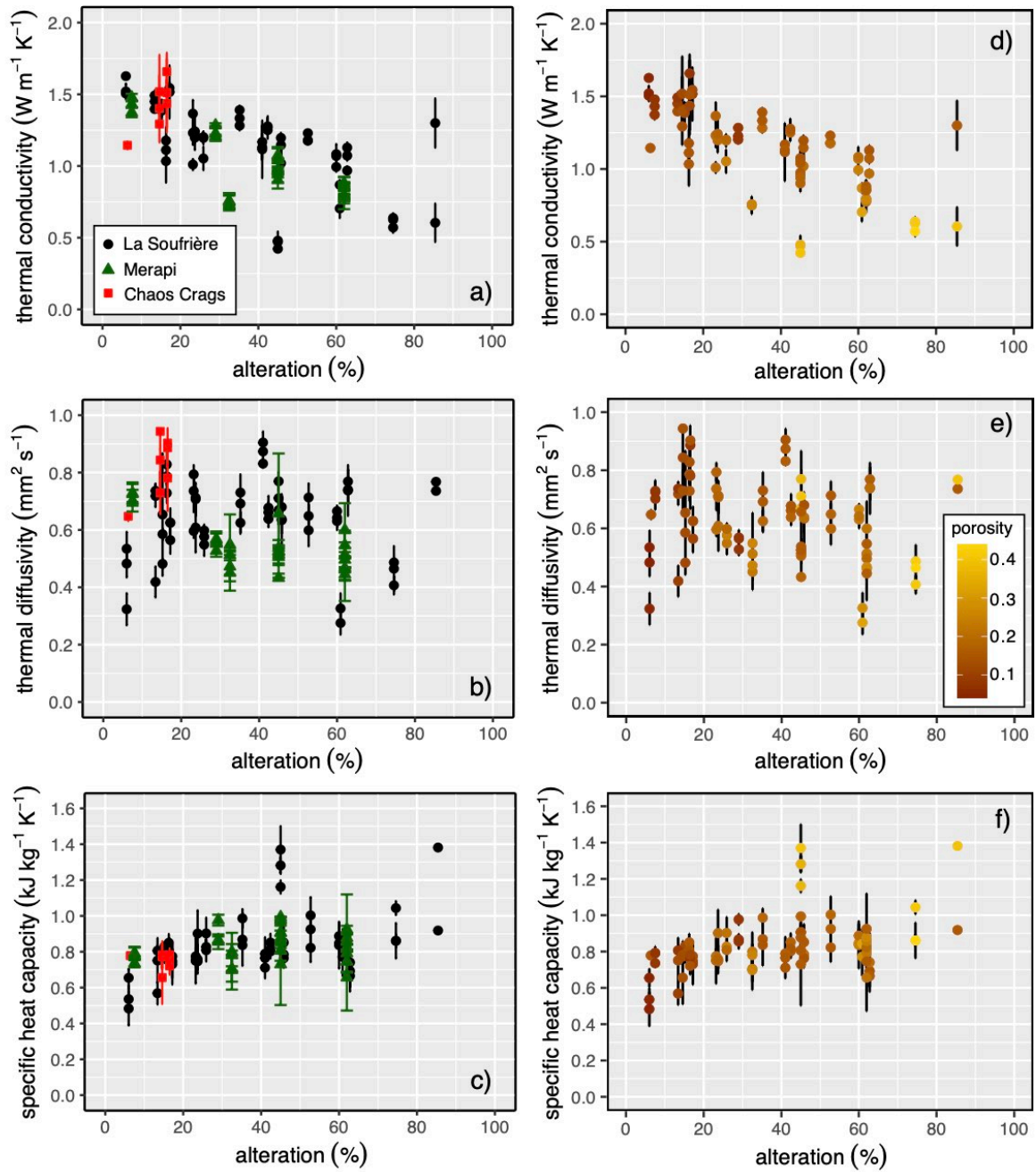
474

**Figure 7.** Thermal conductivity (a and d), thermal diffusivity (b and e), and specific heat capacity (c and f) as a function of connected porosity for the samples from La Soufrière de Guadeloupe (Eastern Caribbean), Merapi volcano (Indonesia; data from Heap et al., 2020a), Ruapehu (New Zealand; data from Heap et al., 2020a), and Chaos Crags (USA). In panels (a–c), the symbols and colours differentiate the data from the different volcanoes (La Soufrière de Guadeloupe: black (rocks) and grey circles (powders); Merapi volcano: green triangles;

475 Ruapehu: blue triangles; Chaos Crag: red squares). In panels (d–f), the colour of the symbol  
476 (where red and yellow indicate low and high values, respectively) indicates the alteration  
477 (percentage of secondary minerals). Numbers next to the modelled curves in panels (a), (b),  
478 (d), and (e) indicate the assumed rock groundmass conductivity,  $\lambda_0$  (in  $\text{W}\cdot\text{m}^{-1}\cdot\text{K}^{-1}$ ). The  
479 modelled curves for  $\lambda_0$  values of 0.85 and 1.9  $\text{W}\cdot\text{m}^{-1}\cdot\text{K}^{-1}$  are designed to bracket the dataset.  
480

## 481 5.2 The influence of alteration on thermal properties

482 To explore the influence of hydrothermal alteration on the thermal properties of volcanic  
483 rocks, we plot thermal conductivity, thermal diffusivity, and specific heat capacity as a function  
484 of alteration (taken to be the weight percentage of secondary minerals) in Figure 8. We  
485 supplement these data with published data for variably-altered basaltic-andesites from Merapi  
486 volcano (from Heap et al., 2020a; Table 3) and new data for variably-altered rhyodacites from  
487 Chaos Crag (Table 3). The methods used, XRPD to quantify their mineral contents and the  
488 Hot Disk® Thermal Constants Analyser to measure their thermal properties, were the same as  
489 for the measured materials from La Soufrière (presented in Table 2), adding confidence to direct  
490 data comparisons. Similar to the samples from La Soufrière, the secondary mineral assemblages  
491 of the rocks from Merapi volcano and Chaos Crag correspond to intermediate to advanced  
492 argillic alteration.



493

494 **Figure 8.** Thermal conductivity (a and d), thermal diffusivity (b and e), and specific heat  
 495 capacity (c and f) as a function of alteration (percentage of secondary minerals) for the  
 496 samples from La Soufrière de Guadeloupe (Eastern Caribbean), Merapi volcano (Indonesia;  
 497 data from Heap et al., 2020a), and Chaos Crags (USA). In panels (a–c), the symbols and  
 498 colours differentiate the data from the different volcanoes (La Soufrière de Guadeloupe: black  
 499 (rocks) and grey circles (powders); Merapi volcano: green triangles; Ruapehu: blue triangles;

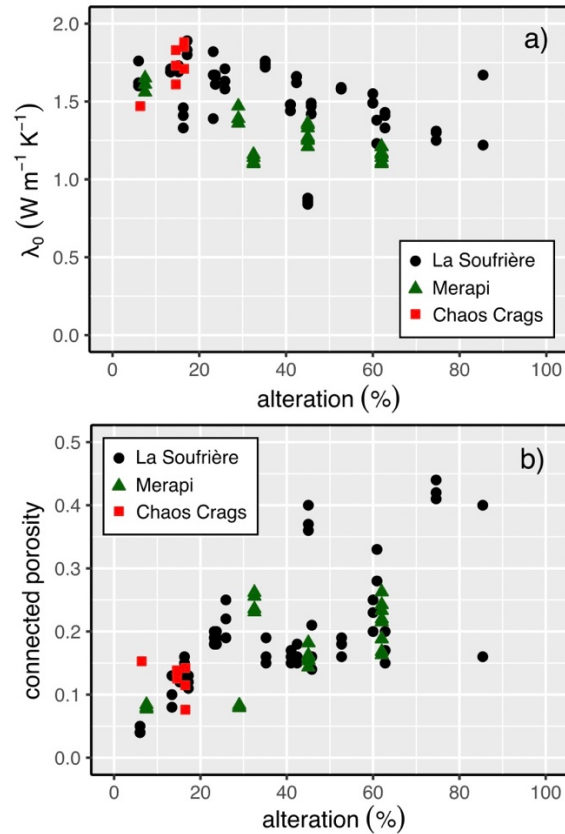
500 Chaos Crags: red squares). In panels (d–f), the colour of the symbol (where red and yellow  
501 indicate low and high values, respectively) indicates the connected porosity.

502

503 The thermal conductivity of the rocks from La Soufrière and Merapi volcano decreases  
504 as a function of increasing alteration, from  $\sim 1.6 \text{ W}\cdot\text{m}^{-1}\cdot\text{K}^{-1}$  at an alteration of  $\sim 1.5 \text{ wt.}\%$  to  
505  $\sim 0.6 \text{ W}\cdot\text{m}^{-1}\cdot\text{K}^{-1}$  at an alteration  $> 75 \text{ wt.}\%$  (Figure 8a). The thermal conductivity of the rocks  
506 from Chaos Crags, on the other hand, increases as alteration increases, from  $\sim 1.1 \text{ W}\cdot\text{m}^{-1}\cdot\text{K}^{-1}$   
507 at an alteration of  $\sim 6 \text{ wt.}\%$  to  $\sim 1.5 \text{ W}\cdot\text{m}^{-1}\cdot\text{K}^{-1}$  at an alteration of  $\sim 15 \text{ wt.}\%$  (Figure 8a).  
508 Although the thermal diffusivity of the rocks from La Soufrière and Merapi volcano does not  
509 appear to be influenced by alteration, the thermal diffusivity of the rocks from Chaos Crags  
510 increases from  $\sim 0.65$  to  $\sim 0.75\text{--}0.95 \text{ mm}^2\cdot\text{s}^{-1}$  as alteration increases from  $\sim 6$  to  $\sim 15 \text{ wt.}\%$  (Figure  
511 8b). The specific heat capacity of all rocks does not appear to be significantly affected by  
512 alteration, although there is a slight trend of increasing specific heat capacity with increasing  
513 alteration for the rocks from La Soufrière (Figure 8c).

514 The reasons for the observed changes in thermal properties as a function of  
515 hydrothermal alteration (Figure 8) are twofold. First, the thermal properties of the primary and  
516 secondary minerals differ (Horai, 1971; Brigaud and Vasseur, 1989; Clauser and Huenges,  
517 1995). Therefore, increasing the proportion of secondary minerals at the expense of the primary  
518 minerals will either increase or decrease the thermal properties of a sample, depending on  
519 whether the secondary minerals have higher values of thermal conductivity, diffusivity, and  
520 specific heat capacity than the primary minerals. Second, hydrothermal alteration can promote  
521 either increases in porosity (dissolution) or decreases in porosity (pore- and crack-filling  
522 mineral precipitation), a physical property known to influence thermal conductivity (as  
523 discussed in the previous section; Figure 5; Robertson and Peck, 1974; Heap et al., 2020a).

524



525

526 **Figure 9.** The thermal conductivity of the rock groundmass,  $\lambda_0$ , calculated using Equation (1)  
 527 (a) and the connected porosity (b) as a function of alteration (percentage of secondary  
 528 minerals) for the samples from La Soufrière de Guadeloupe (Eastern Caribbean; black  
 529 circles), Merapi volcano (Indonesia; green triangles; data from Heap et al., 2020a), and Chaos  
 530 Crags (USA; red squares).

531

532 To explore whether the different thermal properties of secondary minerals, compared to  
 533 primary minerals, is affecting the thermal properties of the studied rocks, we exploit the fact  
 534 that Equation (1) shows that  $\lambda$  is only a function of  $\lambda_0$  (the thermal conductivity of the  
 535 groundmass) and the porosity, such that we can solve for  $\lambda_0$  for each sample. The value of  $\lambda_0$   
 536 for each sample represents the thermal conductivity of the sample at zero porosity, allowing us  
 537 to assess solely the influence of alteration on thermal conductivity.  $\lambda_0$  is plotted as a function  
 538 of alteration in Figure 9a. Figure 9a shows that  $\lambda_0$  broadly decreases as a function of alteration

539 for the samples from La Soufrière and Merapi volcano, but appears to increase for the samples  
540 from Chaos Crag. The decrease in thermal conductivity as a function of alteration for the  
541 samples from La Soufrière and Merapi volcano can be, at least partly, explained by the lower  
542 thermal conductivity of the secondary minerals compared to the primary minerals (Horai, 1971;  
543 Brigaud and Vasseur, 1989; Clauser and Huenges, 1995). For example, the thermal conductivity  
544 of kaolinite, a common replacement mineral in the rocks from La Soufrière (Table 1; Figures 3  
545 and 4), is lower than that of plagioclase (Horai, 1971; Brigaud and Vasseur, 1989). For the rocks  
546 from Chaos Crag, we note that, although smectite and kaolinite have low thermal  
547 conductivities (Brigaud and Vasseur, 1989), the high thermal conductivity of cristobalite ( $\sim 6$   
548  $\text{W}\cdot\text{m}^{-1}\cdot\text{K}^{-1}$ ; Kunugi et al., 1972) could explain why their thermal conductivities appear to  
549 increase as a function of increasing alteration (Figure 8a).

550         The above analysis suggests that hydrothermal alteration can modify the thermal  
551 conductivity of volcanic rock by changing the mineral assemblage. However, alteration can  
552 also result in either increases in porosity (dissolution) or decreases in porosity (pore- and crack-  
553 filling mineral precipitation), a parameter that we have already established as important in  
554 dictating the thermal properties of volcanic rock (Figure 7). To explore whether the observed  
555 alteration as resulted in changes to porosity, and therefore thermal properties, we plot alteration  
556 as a function of porosity in Figure 9b. We also provide plots in Figure 7 that show thermal  
557 conductivity, thermal diffusivity, and specific heat capacity as a function of porosity in which  
558 the symbol colour indicates the alteration (Figures 7d, 7e, and 7f). Similarly, in Figures 8d, 8e,  
559 and 8f, which show plots of thermal conductivity, thermal diffusivity, and specific heat capacity  
560 as a function of alteration, the symbol colour indicates the porosity. Figure 9b shows that  
561 porosity increases as a function of alteration for the rocks from La Soufrière and Merapi  
562 volcano, but appears to decrease as a function of alteration for the rocks from Chaos Crag.  
563 Figures 7d–f and 8d–f also show that the more altered samples are typically the most porous.

564 Therefore, we could conclude from these data that the changes in thermal properties as a  
565 function of alteration (Figure 8a) are also the result of alteration-induced increases (in the case  
566 of the rocks from La Soufrière and Merapi volcano) and decreases (in the case of the rocks from  
567 Chaos Crags) to the porosity, alongside the changes resulting from modifications to the mineral  
568 assemblage (Figure 9a). However, because alteration efficiency is increased by higher fluid-  
569 rock ratios (Giggenbach, 1984), another possibility is that the high-porosity rocks collected  
570 from La Soufrière and Merapi volcano are simply more altered because they were initially more  
571 porous and permeable. We also note that detailed microstructural analysis on the rocks from La  
572 Soufrière (Figures 3 and 4; Heap et al., 2021a) and Merapi volcano (Heap et al., 2019, 2021c)  
573 shows that not all alteration was associated with mineral dissolution, and that samples from  
574 both sample suites show evidence of microcrack- and pore-filling alteration (Figures 3 and 4;  
575 Heap et al., 2019, 2021a). Therefore, although we observe changes in the thermal properties of  
576 the rocks collected from La Soufrière and Merapi volcano as a function of alteration (Figure 8),  
577 it is difficult at present to conclude whether changes in porosity resulting directly from  
578 alteration influenced their thermal properties. It appears more likely, due to the abundance of  
579 void-filling mineral precipitation (Figures 3 and 4; Heap et al., 2021a), that the trend of  
580 increasing porosity with alteration (Figure 9b) is simply the result of increasing alteration  
581 efficiency at higher porosity due to an increase in fluid-rock ratio (i.e. higher interfacial surface  
582 area). Therefore, in the case of the andesites and basaltic-andesites from La Soufrière and  
583 Merapi volcano, it is likely that the decrease in thermal conductivity as a function of alteration  
584 (Figure 8a) is the result of the low conductivity of the secondary mineral assemblage (Horai,  
585 1971; Brigaud and Vasseur, 1989; Clauser and Huenges, 1995).

586         The explanation that higher porosities, and therefore higher fluid-rock ratios, led to more  
587 efficient alteration, however, cannot explain the decrease in porosity as alteration is increased  
588 from ~6 wt.% to ~15 wt.% in the rocks from Chaos Crags (Figure 9b). Detailed microstructural

589 work on the rocks from Chaos Craggs showed that the alteration was manifest as microcrack-  
590 and pore-filling mineral precipitation of mainly cristobalite and kaolinite (Heap et al., 2021b).  
591 Therefore, in the case of the rhyodacites from Chaos Craggs, it is likely that the increase in  
592 thermal conductivity (Figure 8a) and thermal diffusivity (Figure 8b) as alteration is increased  
593 from ~6 to ~15 wt.% is the result of a combination of the high thermal conductivity of  
594 cristobalite and the reduction in porosity as a result of the void-filling mineral precipitation.

595

### 596 5.3 Volcanological implications

597 The heat flux from an active volcano provides crucial information on volcanic unrest  
598 (Jessop et al., 2021) and provides an indication as to the likelihood of magmatic and phreatic  
599 eruptions (Girona et al., 2021). As a result, processes that can alter the thermal properties of  
600 dome- or edifice-forming rocks are of interest to those tasked with interpreting volcano heat  
601 flux data. We have shown here that porosity (Figure 7) and alteration (Figure 8) can influence  
602 the thermal properties of suites of volcanic rocks (basaltic-andesites, andesites, and rhyodacites)  
603 from La Soufrière, Merapi volcano, and Chaos Craggs. The main focus of this contribution is  
604 the influence of alteration on thermal properties.

605 To explore the influence of alteration on the heat output of a dome, we can provide  
606 estimates for the contribution of the heat flux from the dome,  $q$ , from conduction alone using  
607 Fourier's law,

608

$$609 \quad q = -\lambda \frac{dT}{dz} \approx \lambda \frac{\Delta T}{H}, (4)$$

610

611 where  $\lambda$  is the thermal conductivity,  $T$  is the temperature,  $z$  is the vertical position in the dome  
612 ( $z = 0$  is the dome top and  $z = H$  is the base of the dome), and  $\Delta T$  is the difference in  
613 temperature between the top and base of the dome. Although in a real volcanic setting, heat

614 may be transported by a number of additional mechanisms that would represent additional terms  
615 in Equation (4), here we assume that heat transport is by conduction alone, which allows us to  
616 investigate the relative influence of alteration on heat flux. We additionally neglect a  
617 temperature-dependence of  $\lambda$ , which is valid at the relatively low temperatures of edifice rocks  
618 (Whittington et al., 2009; Romaine et al., 2012) and assume that the dome is homogeneous. We  
619 assume at dome height  $H = 200$  m, and a temperature difference  $\Delta T = 300$  °C. Based on our  
620 experimental results (Figure 8a), we consider two scenarios: (1) a scenario in which alteration  
621 decreases the thermal conductivity and (2) a scenario in which alteration increases the thermal  
622 conductivity. For each scenario, we consider three dome states: (1) unaltered, (2) slightly  
623 altered, and (3) altered. For the first scenario we assume thermal conductivities of 1.5, 1, and  
624  $0.5 \text{ W}\cdot\text{m}^{-1}\cdot\text{K}^{-1}$  for the unaltered, slightly altered, and altered dome, respectively (Figure 7a).  
625 And for the second scenario we assume thermal conductivities of 1, 1.25, and  $1.5 \text{ W}\cdot\text{m}^{-1}\cdot\text{K}^{-1}$   
626 for the unaltered, slightly altered, and altered dome, respectively (Figure 8a). The calculated  
627 conductive heat flux for the first scenario are 2.25, 1.5, and  $0.75 \text{ W}\cdot\text{m}^{-2}$ , respectively, and 1.5,  
628 1.875, and  $2.25 \text{ W}\cdot\text{m}^{-2}$  for the second scenario, respectively. These simple calculations should  
629 be considered for illustrative purposes only as they assume (1) that the dome is homogenous in  
630 terms of its thermal conductivity, and (2) there is no temperature dependence of thermal  
631 conductivity, a factor that can influence the thermal properties of volcanic rocks (Whittington  
632 et al., 2009; Romaine et al., 2012). Nevertheless, for conductive heat transport alone, it is clear  
633 from Equation (4) that the alteration-dependence of  $\lambda$  will have a linearly proportional impact  
634 on  $q$ . Our results show that  $\lambda$  can change by up to a factor of three as alteration increases, which  
635 will reduce  $q$  by a third. More importantly, our results suggest that dynamic changes in  $q$   
636 observed directly at volcanoes could represent changes in sub-surface alteration.

637           The mean ground heat flux measured at La Soufrière, for example, was measured to be  
638  $406 \pm 24 \text{ W}\cdot\text{m}^{-2}$  in 2020 (Jessop et al., 2021). Therefore, although alteration-induced changes

639 to the thermal conductivity of the dome can influence the measured heat flux, as discussed  
640 above, the contribution from conduction is likely much less than that from other heat transport  
641 mechanisms, such as the convection of hydrothermal fluids within the core of the edifice;  
642 although we note that conduction becomes the dominant mode of heat transfer between the  
643 condensation isotherm and the surface (Harris, 2013), and that ongoing work at La Soufrière  
644 supports this view (Lebas, 2021). However, changes in porosity resulting from alteration can  
645 also modify permeability (Sruoga et al., 2004; Mayer et al., 2016; Heap et al., 2017b, 2019,  
646 2020b; Revil et al., 2020; Kennedy et al., 2020; Heap et al., 2021b; Kanakiya et al., 2021),  
647 which can influence the efficiency of the migration of hot fluids up through the dome structure  
648 and therefore affect the measured volcano heat flux by increasing or decreasing the influence  
649 of convection. Therefore, alteration can influence volcanic heat flux by changing the thermal  
650 conductivity of the rocks, as explored in this contribution, and also by changing the ease of  
651 convection within the dome by modifying permeability. A full description of heat transfer, in  
652 which conduction and convection are solved together, that also incorporates the influence of  
653 hydrothermal alteration on thermal properties, porosity, and permeability represents the logical  
654 next step in unravelling the influence of alteration on volcano heat flux. Although this complete  
655 description currently eludes us, we conclude with the available data that hydrothermal alteration  
656 can influence volcano heat flux and should therefore be considered when interpreting heat flux  
657 data collected at active volcanoes worldwide.

658

## 659 **6 Conclusions**

660 We have provided laboratory measurements of thermal conductivity, thermal  
661 diffusivity, and specific heat capacity for variably altered volcanic rocks. These data show that  
662 thermal conductivity and thermal diffusivity decrease as a function of porosity, and that specific  
663 heat capacity does not change systematically as a function of porosity (as discussed in Heap et

664 al., 2020a). When plotted as a function of alteration (the percentage of secondary minerals), we  
665 find that thermal conductivity decreases for the rocks from La Soufrière and Merapi volcano,  
666 but appears to increase for the rocks from Chaos Crags. Although the thermal diffusivity of the  
667 rocks from Chaos Crags increases as a function of alteration, the thermal diffusivity of the rocks  
668 from La Soufrière and Merapi volcano does not appear to be influenced by alteration. The  
669 specific heat capacity is not significantly affected by alteration, although there is a slight trend  
670 of increasing specific heat capacity with alteration for the rocks from La Soufrière.

671         We conclude that the decrease in thermal conductivity as a function of alteration in the  
672 rocks from La Soufrière and Merapi volcano is the result of the low conductivity of the  
673 secondary mineral assemblage, and that a combination of the high thermal conductivity of  
674 cristobalite and the reduction in porosity as a result of the void-filling mineral precipitation can  
675 explain the increase in thermal conductivity in the rocks from Chaos Crags.

676         Although Fourier's law shows that an increase in alteration of a dome or edifice can  
677 modify thermal conductivity and therefore heat flux, the contribution from conduction is likely  
678 much less than that from other heat transport mechanisms, such as convection (see, for example,  
679 Jessop et al., 2021). However, we conclude that not only is it important to be aware that  
680 alteration can influence the thermal conductivity of the dome or edifice, but that alteration can  
681 also influence permeability and therefore the convection of heat, a factor that can greatly modify  
682 the heat flux measured at the volcano.

683         Because the heat flux of an active volcano provides crucial information about volcanic  
684 unrest (Jessop et al., 2021; Girona et al., 2021), we conclude that the extent and, importantly, the  
685 type of alteration should be routinely monitored. Monitoring can be performed by remote and/or  
686 ground-based optical and spectroscopic methods (Crowley and Zimbelman, 1997; John et al.,  
687 2008; Darmawan et al., 2018; Kereszturi et al., 2020; Mueller et al., 2021), gas and thermal  
688 monitoring (Edmonds et al., 2003; Tamburello et al., 2019; de Moor et al., 2019; Jessop et al.,

689 2021; Moretti et al., 2020), geological mapping (van Wyk de Vries et al., 2000), magnetic  
690 methods (Finn et al., 2007), deformation monitoring (Moretti et al., 2020), near-surface seismic  
691 imaging (Amoroso et al., 2018), electrical tomography (Ahmed et al., 2018; Byrdina et al.,  
692 2017; Ghorbani et al., 2018; Rosas-Carbajal et al., 2016), and muon tomography (Lesparre et  
693 al., 2012; Rosas-Carbajal et al., 2017). A better understanding of hydrothermal alteration, and  
694 how alteration can influence the thermal properties, porosity, and permeability of dome- and  
695 edifice-forming rock, will allow for a deeper understanding of volcano heat fluxes and therefore  
696 the hazards posed by volcanoes with active hydrothermal systems.

697

## 698 **Acknowledgements**

699 This work was supported by the TelluS Program of INSU-CNRS (“Assessing the role  
700 of hydrothermal alteration on volcanic hazards”) and ANR grant MYGALE (“Modelling the  
701 phYsical and chemical Gradients of hydrothermal ALteration for warning systems of flank  
702 collapse at Explosive volcanoes”), awarded to the first author. M. Heap also acknowledges  
703 support from the Institut Universitaire de France (IUF). We thank the IPGP for general funding  
704 for the Observatoires Volcanologiques et Sismologiques (OVS), INSU-CNRS for the funding  
705 provided by the Service National d’Observation en Volcanologie (SNOV), and the Ministère  
706 pour la Transition Ecologique (MTE) for financial support for the monitoring of the instable  
707 flank of La Soufrière de Guadeloupe. This study contributes to the IdEx Université de Paris  
708 ANR-18-IDEX-0001. We thank Tomaso Esposti Ongaro, Gilles Morvan, and Christophe  
709 Nevado. Material collection from Chaos Crags as permitted by the United States National Park  
710 Service (study: LAVO-00050; permit: LAVO-2019-SCI-0010), and we thank Kelly Russell,  
711 Stephan Kolzenburg, Lori Kennedy, Martin Harris, and Michael Clynne for their help and  
712 support. This is Laboratory of Excellence /ClerVolc /contribution n° 506. We thank two  
713 reviewers for constructive comments that helped improve this manuscript.

714

715 **CRedit author statement**

716 **Michael J. Heap:** Conceptualization; Methodology; Formal analysis; Investigation; Resources;

717 Writing - Original draft; Visualization; Supervision; Project administration; Funding

718 acquisition

719 **David Jessop:** Conceptualization; Investigation; Resources

720 **Marina Rosas-Carbajal:** Investigation; Resources; Project administration; Funding

721 acquisition

722 **Jean-Christophe Komorowski:** Investigation; Resources; Project administration; Funding

723 acquisition

724 **H. Albert Gilg:** Investigation

725 **Nadège Aron:** Investigation

726 **Margaux Buscetti:** Investigation

727 **Laura Gential:** Investigation

728 **Margaux Goupil:** Investigation

729 **Mathilde Masson:** Investigation

730 **Lucie Hervieu:** Investigation

731 **Alexandra R.L. Kushnir:** Methodology; Supervision

732 **Patrick Baud:** Investigation; Resources

733 **Lucille Carbillet:** Investigation; Resources

734 **Amy G. Ryan:** Investigation; Resources

735 **Roberto Moretti:** Resources; Project administration

736

737 **References**

- 738 Ahmed, A. S., Revil, A., Byrdina, S., Coperey, A., Gailler, L., Grobbe, N., ... & Hogg, C.  
739 (2018). 3D electrical conductivity tomography of volcanoes. *Journal of Volcanology and*  
740 *Geothermal Research*, 356, 243-263.
- 741 Allard, P., Aiuppa, A., Beauducel, F., Gaudin, D., Di Napoli, R., Calabrese, S., ... &  
742 Tamburello, G. (2014). Steam and gas emission rate from La Soufriere volcano,  
743 Guadeloupe (Lesser Antilles): implications for the magmatic supply during degassing  
744 unrest. *Chemical Geology*, 384, 76-93.
- 745 Amoroso, O., Festa, G., Bruno, P. P., D'Auria, L., De Landro, G., Di Fiore, V., ... & Zollo, A.  
746 (2018). Integrated tomographic methods for seismic imaging and monitoring of volcanic  
747 caldera structures and geothermal areas. *Journal of Applied Geophysics*, 156, 16-30.
- 748 Annen, C., Pichavant, M., Bachmann, O., & Burgisser, A. (2008). Conditions for the growth of  
749 a long-lived shallow crustal magma chamber below Mount Pelee volcano (Martinique,  
750 Lesser Antilles Arc). *Journal of Geophysical Research: Solid Earth*, 113(B7).
- 751 Annen, C. (2017). Factors affecting the thickness of thermal aureoles. *Frontiers in Earth*  
752 *Science*, 5, 82.
- 753 Bagdassarov, N., & Dingwell, D. (1994). Thermal properties of vesicular rhyolite. *Journal of*  
754 *Volcanology and Geothermal Research*, 60(2), 179-191.
- 755 Bergmann, J., Friedel, P., & Kleeberg, R. (1998). BGMN—a new fundamental parameters  
756 based Rietveld program for laboratory X-ray sources, its use in quantitative analysis and  
757 structure investigations. *CPD Newsletter*, 20(5).
- 758 Bloomberg, S., Werner, C., Rissmann, C., Mazot, A., Horton, T., Gravley, D., ... & Oze, C.  
759 (2014). Soil CO<sub>2</sub> emissions as a proxy for heat and mass flow assessment, Taupō  
760 Volcanic Zone, New Zealand. *Geochemistry, Geophysics, Geosystems*, 15(12), 4885-  
761 4904.
- 762 Boudon, G., Semet, M. P., & Vincent, P. M. (1987). Magma and hydrothermally driven sector  
763 collapses: The 3100 and 11,500 y. BP eruptions of la Grande Decouverte (la Soufriere)  
764 volcano, Guadeloupe, French West Indies. *Journal of Volcanology and Geothermal*  
765 *Research*, 33(4), 317-323.
- 766 Bouligand, C., Coutant, O., & Glen, J. M. (2016). Sub-surface structure of La Soufrière of  
767 Guadeloupe lava dome deduced from a ground-based magnetic survey. *Journal of*  
768 *Volcanology and Geothermal Research*, 321, 171-181.
- 769 Brigaud, F., & Vasseur, G. (1989). Mineralogy, porosity and fluid control on thermal  
770 conductivity of sedimentary rocks. *Geophysical Journal International*, 98(3), 525-542.
- 771 Brombach, T., Marini, L., & Hunziker, J. C. (2000). Geochemistry of the thermal springs and  
772 fumaroles of Basse-Terre Island, Guadeloupe, Lesser Antilles. *Bulletin of Volcanology*,  
773 61(7), 477-490.
- 774 Brothelande, E., Finizola, A., Peltier, A., Delcher, E., Komorowski, J. C., Di Gangi, F., ... &  
775 Legendre, Y. (2014). Fluid circulation pattern inside La Soufrière volcano (Guadeloupe)  
776 inferred from combined electrical resistivity tomography, self-potential, soil temperature  
777 and diffuse degassing measurements. *Journal of Volcanology and Geothermal Research*,  
778 288, 105-122.
- 779 Bruce, P. M., & Huppert, H. E. (1989). Thermal control of basaltic fissure eruptions. *Nature*,  
780 342(6250), 665-667.
- 781 Byrdina, S., Friedel, S., Vandemeulebrouck, J., Budi-Santoso, A., Suryanto, W., Rizal, M. H.,  
782 & Winata, E. (2017). Geophysical image of the hydrothermal system of Merapi volcano.  
783 *Journal of Volcanology and Geothermal Research*, 329, 30-40.
- 784 Carrigan, C. R. (1984). Time and temperature dependent convection models of cooling  
785 reservoirs: Application to volcanic sills. *Geophysical Research Letters*, 11(8), 693-696.

- 786 Carrigan, C. R., Schubert, G., & Eichelberger, J. C. (1992). Thermal and dynamical regimes of  
787 single-and two-phase magmatic flow in dikes. *Journal of Geophysical Research: Solid*  
788 *Earth*, 97(B12), 17377-17392.
- 789 Chiodini, G., Granieri, D., Avino, R., Caliro, S., Costa, A., & Werner, C. (2005). Carbon  
790 dioxide diffuse degassing and estimation of heat release from volcanic and hydrothermal  
791 systems. *Journal of Geophysical Research: Solid Earth*, 110(B8).
- 792 Clauser, C., & Huenges, E. (1995). Thermal conductivity of rocks and minerals. *Rock physics*  
793 *and phase relations: a handbook of physical constants*, 3, 105-126.
- 794 Connor, C. B., Lichtner, P. C., Conway, F. M., Hill, B. E., Ovsyannikov, A. A., Federchenko,  
795 I., ... & Taran, Y. A. (1997). Cooling of an igneous dike 20 yr after intrusion. *Geology*,  
796 25(8), 711-714.
- 797 Crowley, J. K., & Zimelman, D. R. (1997). Mapping hydrothermally altered rocks on Mount  
798 Rainier, Washington, with airborne visible/infrared imaging spectrometer (AVIRIS) data.  
799 *Geology*, 25(6), 559-562.
- 800 Darmawan, H., Walter, T. R., Brotopuspito, K. S., & Nandaka, I. G. M. A. (2018).  
801 Morphological and structural changes at the Merapi lava dome monitored in 2012–15  
802 using unmanned aerial vehicles (UAVs). *Journal of Volcanology and Geothermal*  
803 *Research*, 349, 256-267.
- 804 Dehn, J., Dean, K., & Engle, K. (2000). Thermal monitoring of North Pacific volcanoes from  
805 space. *Geology*, 28(8), 755-758.
- 806 de Moor, J. M., Stix, J., Avard, G., Muller, C., Corrales, E., Diaz, J. A., ... & Fischer, T. P.  
807 (2019). Insights on hydrothermal-magmatic interactions and eruptive processes at Poás  
808 Volcano (Costa Rica) from high-frequency gas monitoring and drone measurements.  
809 *Geophysical Research Letters*, 46(3), 1293-1302.
- 810 Döbelin, N., & Kleeberg, R. (2015). Profex: a graphical user interface for the Rietveld  
811 refinement program BGMN. *Journal of applied crystallography*, 48(5), 1573-1580.
- 812 Edmonds, M., Oppenheimer, C., Pyle, D. M., Herd, R. A., & Thompson, G. (2003). SO<sub>2</sub>  
813 emissions from Soufrière Hills Volcano and their relationship to conduit permeability,  
814 hydrothermal interaction and degassing regime. *Journal of Volcanology and Geothermal*  
815 *Research*, 124(1-2), 23-43.
- 816 Feuillard, M., Allègre, C. J., Brandeis, G., Gaulon, R., Le Mouel, J. L., Mercier, J. C., ... &  
817 Semet, M. P. (1983). The 1975–1977 crisis of La Soufrière de Guadeloupe (FWI): a still-  
818 born magmatic eruption. *Journal of Volcanology and Geothermal Research*, 16(3-4), 317-  
819 334.
- 820 Fialko, Y. A., & Rubin, A. M. (1999). Thermal and mechanical aspects of magma emplacement  
821 in giant dike swarms. *Journal of Geophysical Research: Solid Earth*, 104(B10), 23033-  
822 23049.
- 823 Finn, C. A., Deszcz-Pan, M., Ball, J. L., Bloss, B. J., & Minsley, B. J. (2018). Three-  
824 dimensional geophysical mapping of shallow water saturated altered rocks at Mount  
825 Baker, Washington: Implications for slope stability. *Journal of Volcanology and*  
826 *Geothermal Research*, 357, 261-275.
- 827 Fujii, N., & Osako, M. (1973). Thermal diffusivity of lunar rocks under atmospheric and  
828 vacuum conditions. *Earth and Planetary Science Letters*, 18(1), 65-71.
- 829 Gaudin, D., Beauducel, F., Allemand, P., Delacourt, C., & Finizola, A. (2013). Heat flux  
830 measurement from thermal infrared imagery in low-flux fumarolic zones: Example of the  
831 Ty fault (La Soufrière de Guadeloupe). *Journal of Volcanology and Geothermal*  
832 *Research*, 267, 47-56.
- 833 Ghorbani, A., Revil, A., Coperey, A., Ahmed, A. S., Roque, S., Heap, M. J., ... & Viveiros, F.  
834 (2018). Complex conductivity of volcanic rocks and the geophysical mapping of  
835 alteration in volcanoes. *Journal of Volcanology and Geothermal Research*, 357, 106-127.

836 Giggenbach, W. F. (1984). Mass transfer in hydrothermal alteration systems—a conceptual  
837 approach. *Geochimica et Cosmochimica Acta*, 48(12), 2693-2711.

838 Girona, T., Realmuto, V., & Lundgren, P. (2021). Large-scale thermal unrest of volcanoes for  
839 years prior to eruption. *Nature Geoscience*, 14(4), 238-241.

840 Gustavsson, M., Karawacki, E., & Gustafsson, S. E. (1994). Thermal conductivity, thermal  
841 diffusivity, and specific heat of thin samples from transient measurements with hot disk  
842 sensors. *Review of Scientific Instruments*, 65(12), 3856-3859.

843 Gustafsson, S. E. (1991). Transient plane source techniques for thermal conductivity and  
844 thermal diffusivity measurements of solid materials. *Review of scientific instruments*,  
845 62(3), 797-804.

846 Hammerschmidt, U., & Sabuga, W. (2000). Transient hot strip (THS) method: uncertainty  
847 assessment. *International Journal of Thermophysics*, 21(1), 217-248.

848 Harlé, P., Kushnir, A. R., Aichholzer, C., Heap, M. J., Hehn, R., Maurer, V., ... & Düringer, P.  
849 (2019). Heat flow density estimates in the Upper Rhine Graben using laboratory  
850 measurements of thermal conductivity on sedimentary rocks. *Geothermal Energy*, 7(1),  
851 1-36.

852 Harris, A. J., Blake, S., Rothery, D. A., & Stevens, N. F. (1997). A chronology of the 1991 to  
853 1993 Mount Etna eruption using advanced very high resolution radiometer data:  
854 Implications for real-time thermal volcano monitoring. *Journal of Geophysical Research:*  
855 *Solid Earth*, 102(B4), 7985-8003.

856 Harris, A. J. L., Pilger, E., Flynn, L. P., Garbeil, H., Mouginiis-Mark, P. J., Kauahikaua, J., &  
857 Thornber, C. (2001). Automated, high temporal resolution, thermal analysis of Kilauea  
858 volcano, Hawai'i, using GOES satellite data. *International Journal of Remote Sensing*,  
859 22(6), 945-967.

860 Harris, A. (2013). *Thermal remote sensing of active volcanoes: a user's manual*. Cambridge  
861 University Press.

862 Heap, M. J., & Kennedy, B. M. (2016). Exploring the scale-dependent permeability of fractured  
863 andesite. *Earth and Planetary Science Letters*, 447, 139-150.

864 Heap, M. J., Violay, M., Wadsworth, F. B., & Vasseur, J. (2017a). From rock to magma and  
865 back again: the evolution of temperature and deformation mechanism in conduit margin  
866 zones. *Earth and Planetary Science Letters*, 463, 92-100.

867 Heap, M. J., Kennedy, B. M., Farquharson, J. I., Ashworth, J., Mayer, K., Letham-Brake, M.,  
868 ... & Dingwell, D. B. (2017b). A multidisciplinary approach to quantify the permeability  
869 of the Whakaari/White Island volcanic hydrothermal system (Taupo Volcanic Zone, New  
870 Zealand). *Journal of Volcanology and Geothermal Research*, 332, 88-108.

871 Heap, M. J., Troll, V. R., Kushnir, A. R., Gilg, H. A., Collinson, A. S., Deegan, F. M., ... &  
872 Walter, T. R. (2019). Hydrothermal alteration of andesitic lava domes can lead to  
873 explosive volcanic behaviour. *Nature Communications*, 10(1), 1-10.

874 Heap, M. J., Kushnir, A. R., Vasseur, J., Wadsworth, F. B., Harlé, P., Baud, P., ... & Deegan,  
875 F. M. (2020a). The thermal properties of porous andesite. *Journal of Volcanology and*  
876 *Geothermal Research*, 398, 106901.

877 Heap, M. J., Gravley, D. M., Kennedy, B. M., Gilg, H. A., Bertolett, E., & Barker, S. L. (2020b).  
878 Quantifying the role of hydrothermal alteration in creating geothermal and epithermal  
879 mineral resources: the Ohakuri ignimbrite (Taupō Volcanic Zone, New Zealand). *Journal*  
880 *of Volcanology and Geothermal Research*, 390, 106703.

881 Heap, M. J., Baumann, T. S., Rosas-Carbajal, M., Komorowski, J. C., Gilg, H. A., Villeneuve,  
882 M., ... & Reuschlé, T. (2021a). Alteration-induced volcano instability at La Soufrière de  
883 Guadeloupe (Eastern Caribbean). *Journal of Geophysical Research: Solid Earth*,  
884 e2021JB022514.

885 Heap, M. J., Baumann, T., Gilg, H. A., Kolzenburg, S., Ryan, A. G., Villeneuve, M., ... &  
886 Clynne, M. A. (2021b). Hydrothermal alteration can result in pore pressurization and  
887 volcano instability. *Geology*, <https://doi.org/10.1130/G49063.1>.

888 Heap, M. J., Wadsworth, F. B., Heng, Z., Xu, T., Griffiths, L., Velasco, A. A., ... & Deegan, F.  
889 M. (2021c). The tensile strength of volcanic rocks: Experiments and models. *Journal of*  
890 *Volcanology and Geothermal Research*, 418, 107348.

891 Heap, M. J., & Violay, M. E. (2021). The mechanical behaviour and failure modes of volcanic  
892 rocks: a review. *Bulletin of Volcanology*, 83(5), 1-47.

893 Hincks, T. K., Komorowski, J. C., Sparks, S. R., & Aspinall, W. P. (2014). Retrospective  
894 analysis of uncertain eruption precursors at La Soufrière volcano, Guadeloupe, 1975–77:  
895 volcanic hazard assessment using a Bayesian Belief Network approach. *Journal of*  
896 *Applied Volcanology*, 3(1), 1-26.

897 Hofmeister, A. M. (2019). *Measurements, mechanisms, and models of heat transport*. Elsevier.

898 Horai, K., Simmons, G., Kanamori, H., & Wones, D. (1970). Thermal diffusivity, conductivity  
899 and thermal inertia of Apollo 11 lunar material. *Geochimica et Cosmochimica Acta*  
900 *Supplement*, 1, 2243.

901 Horai, K. I. (1971). Thermal conductivity of rock-forming minerals. *Journal of Geophysical*  
902 *Research*, 76(5), 1278-1308.

903 Irvine, T. N. (1970). Heat transfer during solidification of layered intrusions. I. Sheets and sills.  
904 *Canadian Journal of Earth Sciences*, 7(4), 1031-1061.

905 Jessop, D. E., Moune, S., Moretti, R., Gibert, D., Komorowski, J. C., Robert, V., ... & Burtin,  
906 A. (2021). A multi-decadal view of the heat and mass budget of a volcano in unrest: La  
907 Soufrière de Guadeloupe (French West Indies). *Bulletin of Volcanology*, 83(3), 1-19.

908 John, D. A., Sisson, T. W., Breit, G. N., Rye, R. O., & Vallance, J. W. (2008). Characteristics,  
909 extent and origin of hydrothermal alteration at Mount Rainier Volcano, Cascades Arc,  
910 USA: Implications for debris-flow hazards and mineral deposits. *Journal of Volcanology*  
911 *and Geothermal Research*, 175(3), 289-314.

912 Kanakiya, S., Adam, L., Rowe, M. C., Lindsay, J. M., & Esteban, L. (2021). The role of tuffs  
913 in sealing volcanic conduits. *Geophysical Research Letters*, e2021GL095175.

914 Kennedy, B. M., Farquhar, A., Hilderman, R., Villeneuve, M. C., Heap, M. J., Mordensky, S.,  
915 ... & Reuschlé, T. (2020). Pressure controlled permeability in a conduit filled with  
916 fractured hydrothermal breccia reconstructed from ballistics from Whakaari (White  
917 Island), New Zealand. *Geosciences*, 10(4), 138.

918 Kereszturi, G., Schaefer, L. N., Miller, C., & Mead, S. (2020). Hydrothermal Alteration on  
919 Composite Volcanoes: Mineralogy, Hyperspectral Imaging, and Aeromagnetic Study of  
920 Mt Ruapehu, New Zealand. *Geochemistry, Geophysics, Geosystems*, 21(9),  
921 e2020GC009270.

922 Komorowski, J.-C., Boudon, G., Semet, M., Beauducel, F., Anténor-Habazac, C., Bazin, S., &  
923 Hammouya, G. (2005). Guadeloupe. In: *Volcanic Atlas of the Lesser Antilles* (Eds:  
924 Lindsay, J., Robertson, R., Shepherd, J., & Ali, S.), University of the French West Indies,  
925 Seismic Research Unit, pp. 65-102.

926 Komorowski, J.-C., Hincks, T., Sparks, R., Aspinall, W., & CASAVA ANR Project  
927 Consortium. (2015). Improving crisis decision-making at times of uncertain volcanic  
928 unrest (Guadeloupe, 1976). In: *Global Volcanic Hazards and Risk* (Eds: Loughlin, S.C.,  
929 Sparks, R.S.J., Brown, S.K., Jenkins, S.F., & Vye-Brown, C), Cambridge University  
930 Press, pp 255-261.

931 Kunugi, M., Soga, N., Sawa, H., & Konishi, A. (1972). Thermal conductivity of cristobalite.  
932 *Journal of the American Ceramic Society*, 55(11), 580-580.

- 933 Lebas, F. (2021). Etude du dégazage et de la perte de chaleur du système hydrothermal de La  
934 Soufrière de Guadeloupe : implications pour la surveillance volcanique. Master thesis.  
935 Université de Paris-IPGP.
- 936 Le Friant, A., Boudon, G., Komorowski, J. C., Heinrich, P., & Semet, M. P. (2006). Potential  
937 flank-collapse of Soufrière volcano, Guadeloupe, Lesser Antilles? Numerical simulation  
938 and hazards. *Natural Hazards*, 39(3), 381.
- 939 Lesparre, N., Gibert, D., Marteau, J., Komorowski, J. C., Nicollin, F., & Coutant, O. (2012).  
940 Density muon radiography of La Soufriere of Guadeloupe volcano: comparison with  
941 geological, electrical resistivity and gravity data. *Geophysical Journal International*,  
942 190(2), 1008-1019.
- 943 Mannini, S., Harris, A. J., Jessop, D. E., Chevrel, M. O., & Ramsey, M. S. (2019). Combining  
944 Ground-and ASTER-Based Thermal Measurements to Constrain Fumarole Field Heat  
945 Budgets: The Case of Vulcano Fossa 2000–2019. *Geophysical Research Letters*, 46(21),  
946 11868-11877.
- 947 Mattsson, T., Burchardt, S., Almqvist, B. S., & Ronchin, E. (2018). Syn-emplacement  
948 fracturing in the Sandfell laccolith, eastern Iceland—Implications for rhyolite intrusion  
949 growth and volcanic hazards. *Frontiers in Earth Science*, 6, 5.
- 950 Mayer, K., Scheu, B., Montanaro, C., Yilmaz, T. I., Isaia, R., Aßbichler, D., & Dingwell, D. B.  
951 (2016). Hydrothermal alteration of surficial rocks at Solfatara (Campi Flegrei):  
952 Petrophysical properties and implications for phreatic eruption processes. *Journal of*  
953 *Volcanology and Geothermal Research*, 320, 128-143.
- 954 Mielke, P., Nehler, M., Bignall, G., & Sass, I. (2015). Thermo-physical rock properties and the  
955 impact of advancing hydrothermal alteration—A case study from the Tauhara geothermal  
956 field, New Zealand. *Journal of Volcanology and Geothermal Research*, 301, 14-28.
- 957 Mielke, P., Weinert, S., Bignall, G., & Sass, I. (2016). Thermo-physical rock properties of  
958 greywacke basement rock and intrusive lavas from the Taupo Volcanic Zone, New  
959 Zealand. *Journal of Volcanology and Geothermal Research*, 324, 179-189.
- 960 Mielke, P., Bär, K., & Sass, I. (2017). Determining the relationship of thermal conductivity and  
961 compressional wave velocity of common rock types as a basis for reservoir  
962 characterization. *Journal of Applied Geophysics*, 140, 135-144.
- 963 Moretti, R., Komorowski, J. C., Ucciani, G., Moune, S., Jessop, D., de Chabaliere, J. B., ... &  
964 Chaussidon, M. (2020). The 2018 unrest phase at La Soufrière of Guadeloupe (French  
965 West Indies) andesitic volcano: Scrutiny of a failed but prodromal phreatic eruption.  
966 *Journal of Volcanology and Geothermal Research*, 393, 106769.
- 967 Mueller, D., Bredemeyer, S., Zorn, E., De Paolo, E., & Walter, T. R. (2021). Surveying  
968 fumarole sites and hydrothermal alteration by unoccupied aircraft systems (UAS) at the  
969 La Fossa cone, Vulcano Island (Italy). *Journal of Volcanology and Geothermal Research*,  
970 413, 107208.
- 971 Nabelek, P. I., Hofmeister, A. M., & Whittington, A. G. (2012). The influence of temperature-  
972 dependent thermal diffusivity on the conductive cooling rates of plutons and temperature-  
973 time paths in contact aureoles. *Earth and Planetary Science Letters*, 317, 157-164.
- 974 Nicollin, F., Gibert, D., Beauducel, F., Boudon, G., & Komorowski, J. C. (2006). Electrical  
975 tomography of La Soufrière of Guadeloupe Volcano: Field experiments, 1D inversion  
976 and qualitative interpretation. *Earth and Planetary Science Letters*, 244(3-4), 709-724.
- 977 Norton, D., & Knight, J. (1977). Transport phenomena in hydrothermal systems: cooling  
978 plutons. *Am. J. Sci.:(United States)*, 277.
- 979 Peruzzetto, M., Komorowski, J. C., Le Friant, A., Rosas-Carbajal, M., Mangeney, A., &  
980 Legendre, Y. (2019). Modeling of partial dome collapse of La Soufrière of Guadeloupe  
981 volcano: implications for hazard assessment and monitoring. *Scientific reports*, 9(1), 1-  
982 15.

- 983 Revil, A., Coperey, A., Heap, M. J., & Carbillet, L. (2020). A geophysical index to map  
984 alteration, permeability, and mechanical properties within volcanoes. Application to the  
985 soft volcanic rocks from Whakaari/White Island (New Zealand). *Journal of Volcanology  
986 and Geothermal Research*, 401, 106945.
- 987 Robertson, E. C., & Peck, D. L. (1974). Thermal conductivity of vesicular basalt from Hawaii.  
988 *Journal of Geophysical Research*, 79(32), 4875-4888.
- 989 Romine, W. L., Whittington, A. G., Nabelek, P. I., & Hofmeister, A. M. (2012). Thermal  
990 diffusivity of rhyolitic glasses and melts: effects of temperature, crystals and dissolved  
991 water. *Bulletin of volcanology*, 74(10), 2273-2287.
- 992 Rosas-Carbajal, M., Komorowski, J. C., Nicollin, F., & Gibert, D. (2016). Volcano electrical  
993 tomography unveils edifice collapse hazard linked to hydrothermal system structure and  
994 dynamics. *Scientific Reports*, 6(1), 1-11.
- 995 Rosas-Carbajal, M., Jourde, K., Marteau, J., Deroussi, S., Komorowski, J. C., & Gibert, D.  
996 (2017). Three-dimensional density structure of La Soufrière de Guadeloupe lava dome  
997 from simultaneous muon radiographies and gravity data. *Geophysical Research Letters*,  
998 44(13), 6743-6751.
- 999 Ryan, A. G., Heap, M. J., Russell, J. K., Kennedy, L. A., & Clynne, M. A. (2020). Cyclic shear  
1000 zone cataclasis and sintering during lava dome extrusion: Insights from Chaos Crags,  
1001 Lassen Volcanic Center (USA). *Journal of Volcanology and Geothermal Research*, 401,  
1002 106935.
- 1003 Salaün, A., Villemant, B., Gérard, M., Komorowski, J. C., & Michel, A. (2011). Hydrothermal  
1004 alteration in andesitic volcanoes: trace element redistribution in active and ancient  
1005 hydrothermal systems of Guadeloupe (Lesser Antilles). *Journal of Geochemical  
1006 Exploration*, 111(3), 59-83.
- 1007 Sruoga, P., Rubinstein, N., & Hinterwimmer, G. (2004). Porosity and permeability in volcanic  
1008 rocks: a case study on the Serie Tobífera, South Patagonia, Argentina. *Journal of  
1009 Volcanology and Geothermal Research*, 132(1), 31-43.
- 1010 Stevenson, J. A., & Varley, N. (2008). Fumarole monitoring with a handheld infrared camera:  
1011 Volcán de Colima, Mexico, 2006–2007. *Journal of Volcanology and Geothermal  
1012 Research*, 177(4), 911-924.
- 1013 Tamburello, G., Moune, S., Allard, P., Venugopal, S., Robert, V., Rosas-Carbajal, M., ... &  
1014 Moretti, R. (2019). Spatio-temporal relationships between fumarolic activity,  
1015 hydrothermal fluid circulation and geophysical signals at an arc volcano in degassing  
1016 unrest: La Soufrière of Guadeloupe (French West Indies). *Geosciences*, 9(11), 480.
- 1017 Torquato, S., & Haslach Jr, H. W. (2002). Random heterogeneous materials: microstructure  
1018 and macroscopic properties. *Appl. Mech. Rev.*, 55(4), B62-B63.
- 1019 Tsang, S. W., Lindsay, J. M., Coco, G., Wysocki, R., Lerner, G. A., Rader, E., ... & Kennedy,  
1020 B. (2019). The heating of substrates beneath basaltic lava flows. *Bulletin of Volcanology*,  
1021 81(11), 1-14.
- 1022 van Wyk de Vries, B., Kerle, N., & Petley, D. (2000). Sector collapse forming at Casita volcano,  
1023 Nicaragua. *Geology*, 28(2), 167-170.
- 1024 Vasseur, J., Wadsworth, F. B., Lavallée, Y., & Dingwell, D. B. (2016). Dynamic elastic moduli  
1025 during isotropic densification of initially granular media. *Geophysical Journal  
1026 International*, 204(3), 1721-1728.
- 1027 Vélez, M. I., Blessent, D., Córdoba, S., López-Sánchez, J., Raymond, J., & Parra-Palacio, E.  
1028 (2018). Geothermal potential assessment of the Nevado del Ruiz volcano based on rock  
1029 thermal conductivity measurements and numerical modeling of heat transfer. *Journal of  
1030 South American Earth Sciences*, 81, 153-164.
- 1031 Villemant, B., Hammouya, G., Michel, A., Semet, M. P., Komorowski, J. C., Boudon, G., &  
1032 Cheminée, J. L. (2005). The memory of volcanic waters: shallow magma degassing

- 1033 revealed by halogen monitoring in thermal springs of La Soufrière volcano (Guadeloupe,  
1034 Lesser Antilles). *Earth and Planetary Science Letters*, 237(3-4), 710-728.
- 1035 Villemant, B., Komorowski, J. C., Dessert, C., Michel, A., Crispi, O., Hammouya, G., ... & De  
1036 Chabaliér, J. B. (2014). Evidence for a new shallow magma intrusion at La Soufrière of  
1037 Guadeloupe (Lesser Antilles): insights from long-term geochemical monitoring of  
1038 halogen-rich hydrothermal fluids. *Journal of Volcanology and Geothermal Research*, 285,  
1039 247-277.
- 1040 Whittington, A. G., Hofmeister, A. M., & Nabelek, P. I. (2009). Temperature-dependent  
1041 thermal diffusivity of the Earth's crust and implications for magmatism. *Nature*,  
1042 458(7236), 319-321.
- 1043 Wooster, M. J., & Rothery, D. A. (1997). Thermal monitoring of Lascar Volcano, Chile, using  
1044 infrared data from the along-track scanning radiometer: a 1992–1995 time series. *Bulletin  
1045 of Volcanology*, 58(7), 566-579.
- 1046 Wooster, M. J., Wright, R., Blake, S., & Rothery, D. A. (1997). Cooling mechanisms and an  
1047 approximate thermal budget for the 1991–1993 Mount Etna lava flow. *Geophysical  
1048 Research Letters*, 24(24), 3277-3280.
- 1049 Wright, R., & Flynn, L. P. (2004). Space-based estimate of the volcanic heat flux into the  
1050 atmosphere during 2001 and 2002. *Geology*, 32(3), 189-192.
- 1051 Wright, R., Flynn, L. P., Garbeil, H., Harris, A. J., & Pilger, E. (2004). MODVOLC: near-real-  
1052 time thermal monitoring of global volcanism. *Journal of Volcanology and Geothermal  
1053 Research*, 135(1-2), 29-49.
- 1054 Weydt, L. M., Ramírez-Guzmán, Á. A., Pola, A., Lepillier, B., Kummerow, J., Mandrone, G.,  
1055 ... & Sass, I. (2021). Petrophysical and mechanical rock property database of the Los  
1056 Humeros and Aocolco geothermal fields (Mexico). *Earth System Science Data*, 13(2),  
1057 571-598.
- 1058 Zimmerman, R. W. (1989). Thermal conductivity of fluid-saturated rocks. *Journal of Petroleum  
1059 Science and Engineering*, 3(3), 219-227.